nature cardiovascular research

Article

https://doi.org/10.1038/s44161-025-00755-6

A disrupted compartment boundary underlies abnormal cardiac patterning and congenital heart defects

Received: 15 March 2024

Accepted: 4 November 2025

Published online: 29 December 2025

Check for updates

Irfan S. Kathiriya[1,21] ✉, Martin H. Dominguez[2,3,13], Kavitha S. Rao[1,2], Jonathon M. Muncie-Vasic[2], W. Patrick Devine[2,14], Kevin M. Hu[1,2,15], Swetansu K. Hota[2,16], Bayardo I. Garay[1,17], Diego Quintero[2,18], Piyush Goyal[1,2,19], Megan N. Matthews[1,20], Reuben Thomas[2], Tatyana Sukonnik[2,22], Dario Miguel-Perez[2], Sarah Winchester[2], Emily F. Brower[2], André Forjaz[4], Pei-Hsun Wu[4], Denis Wirtz[4], Ashley L. Kiemen[4,5,6,7] & Benoit G. Bruneau[2,8,9,10,11,12,21] ✉

Failure of septation of the interventricular septum (IVS) is the most common congenital heart defect, but mechanisms for patterning the IVS are largely unknown. Here we show that a *Tbx5*$^{+}$/*Mef2cAHF*$^{+}$ progenitor lineage forms a compartment boundary bisecting the IVS. This coordinated population originates at a first and second heart field interface. Ablation of *Tbx5*$^{+}$/*Mef2cAHF*$^{+}$ progenitors causes IVS disorganization, right ventricular hypoplasia and mixing of IVS lineages. Reduced dosage of the congenital heart defect transcription factor TBX5 disrupts boundary position and integrity, resulting in ventricular septation defects and patterning defects, including misexpression of *Slit2* and *Ntn1*, which encode guidance cues. Reducing NTN1 dosage partly rescues cardiac defects in *Tbx5* mutant embryos. Loss of *Slit2* or *Ntn1* causes ventricular septation defects and perturbed septal lineage distributions. Thus, we identify *Tbx5* as a candidate selector gene, directing progenitors and regulating essential cues, to pattern a compartment boundary for proper cardiac septation, revealing mechanisms for cardiac birth defects.

Organogenesis relies on fine tissue patterning, and disturbances cause organ malformations that result in birth defects. Examples of prevalent birth defects resulting from abnormal patterning include congenital limb abnormalities, neural tube defects or congenital heart defects (CHDs).

CHDs are the most common birth defects and a leading cause of morbidity and mortality in childhood[1]. CHDs are thought to result from alterations to the orchestrated patterning of heart development. Nearly half of all patients with CHDs have atrial septal defects (ASDs) or ventricular septal defects (VSDs), which are abnormalities of the formation of the interventricular septum (IVS)[2,3]. Septal defects can occur either in isolation or combined with other anatomic defects, including abnormal chamber formation. For example, atrioventricular (AV) canal defects include VSDs, ASDs and abnormal development of the AV valves, with severe cases leading to chamber hypoplasia and functional single ventricle physiology[4]. There is a large gap in our understanding of how early developmental events pattern cardiac morphogenesis and anatomy. Addressing this understudied need can inform diagnostic prognosis, family planning and therapeutic approaches for CHDs.

Complete AV septation into four chambers allows for the separation of systemic and pulmonary circulations, and enables higher levels of oxygen to be transported in arterial blood. Although formation of the

A full list of affiliations appears at the end of the paper. ✉e-mail: irfan.kathiriya@ucsf.edu; benoit.bruneau@gladstone.ucsf.edu

https://doi.org/10.1038/s44161-025-00755-6

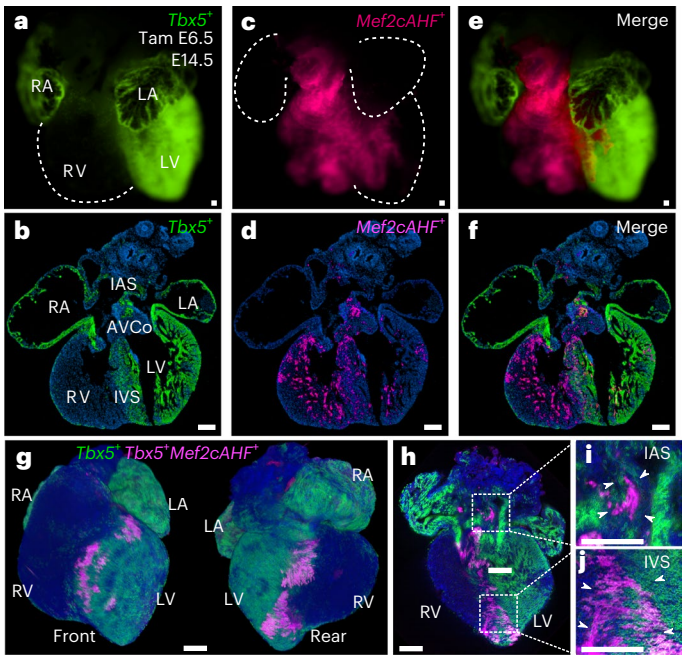

Fig. 1 | *Tbx5*$^{+}$*/Mef2cAHF*$^{+}$ lineage marks a compartment boundary at the cardiac IVS. a,**b**, At E14.5, clonal cell descendants of a *Tbx5*$^{+}$ lineage (ZsGreen) labeled at E6.5 contribute to the LV. Tam, tamoxifen; RA, right atrium; LA, left atrium. **c**,**d**, A *Mef2cAHF*$^{+}$ lineage (tdTomato immunostaining) contributes to the RV, showing largely complementary patterns. **e**, These lineages overlap (*Tbx5*$^{+}$*/Mef2cAHF*$^{+}$) at the IVS, as well as the AVCo region, and IAS. *Tbx5*$^{CreERT2/+}$; *Mef2cAHF-DreERT2*;*ROSA26*$^{Ai6/Ai66b}$ hearts shown using epifluorescence microscopy (**a**, **c** and **e**; scale bars, 200 µm) and cryosections (**b**, **d** and **f**; scale bars: 100 µm). **g**–**j**, Maximal projection images by lightsheet microscopy of an intersectional reporter for the *Tbx5*$^{+}$*/Mef2cAHF*$^{+}$ lineage (tdTomato immunostaining) in *Tbx5*$^{CreERT2/+}$;*Mef2cAHF-DreERT2*;*ROSA26*$^{Ai66/+}$ embryos at E14.5. Scale bars, 200 µm.

IVS, which separates the left ventricle (LV) and right ventricle (RV), is an intricate and poorly understood process, some progress has been made in determining the embryonic origins of the IVS. Dye-labeling studies in chicks have shown that the IVS is derived from the bulbo-ventricular region between the future RV and LV[5], and both the RV and LV supply compact layer cells and some lateral trabecular cells to form the core of the IVS[6–8]. Likewise, discovery of the ganglion nodosum epitope from chicks, which demarcates the primary interventricular (IV) foramen and subsequently the IVS, AV junction and ventricular conduction system in mice, chicks and humans, has led to the description of a 'primary ring' for the ventricular septum[9–11]. Consistent with the primary ring, the cell behavior of IVS primordia shows circumferential-oriented cell growth from the IV groove at the outer curvature to the inner curvature at embryonic day (E) 10.5 (E10.5)[12]. In addition, some gene expression domains are enriched in the IVS. For example, *Tbx5* is expressed in the LV and IVS, and proper TBX5 dosage is essential for IVS formation[13]. *Irx2* is expressed in the IVS and adjacent ventricular tissue[14], and *Lyz2* is expressed at the bulbo-ventricular groove at E9.5 at the site of the future IVS[15]. Furthermore, the *Lyz2*$^{+}$ lineage contributes cells to the muscular portion throughout the developing IVS[15]. This evidence delineates the embryonic origins of the IVS as a distinct region of the developing heart, although its earliest progenitors and regulation are unclear.

Studies have suggested that the linear heart tube is organized into specific segments[16,17], including the IVS[5,18]. It is increasingly apparent in the developing mouse heart that discrete early cardiac progenitors in mesoderm are already fated to contribute to the regionalization of specific cardiac anatomy[19–26]. The first heart field gives rise primarily to the LV and parts of the atria, while the second heart field contributes predominantly to the RV, outflow tract (OFT) and portions of the atria[21]. The heart fields can be largely recapitulated by marking lineage-labeled progenitors at gastrulation[24,25]. Specifically, a cell lineage labeled by the CHD-linked transcription factor *Tbx5* (*Tbx5*$^{+}$ lineage) contributes to the LV, IVS and atria, while the anterior heart field enhancer of *Mef2c* (*Mef2cAHF*$^{+}$) lineage largely contributes to the RV, IVS and OFT[25].

An aspect of proper tissue patterning entails the establishment of compartment boundaries to separate neighboring fields of cells that show discrete functions[27–29]. Few compartment boundaries have been identified in mammals, notably the dorso-ventral patterning of the limb[30–32] and the midbrain–hindbrain boundary[33]. In the developing mouse heart, retrospective clonal cell analysis shows segregation of LV and RV lineages on either the left or right side of the IVS, establishing a presumptive mutual border between the two non-intermingling compartments[12,25,34], reminiscent of a compartment boundary. Moreover, this evidence has led to a prediction of a compartment boundary at the IVS that acts as a barrier to cell mixing between the LV and RV[12,25,34]. Using an intersectional-lineage labeling approach, a subset of cardiac progenitor cells labeled by both *Tbx5*$^{+}$*/Mef2cAHF*$^{+}$ were described with contributions to the left side of the IVS, delineating a cell lineage of an apparent compartment boundary[25]. Understanding the roles of a *Tbx5*$^{+}$*/Mef2cAHF*$^{+}$ lineage-labeled compartment boundary at the IVS may reveal clues about IVS patterning with potential relevance for VSD etiologies. More broadly, how disturbances to compartment boundaries contribute to birth defects is largely unknown.

Here we combined genetic lineage labeling with lightsheet microscopy to follow contributions of *Tbx5*$^{+}$*/Mef2cAHF*$^{+}$ precursors to a compartment boundary during cardiac morphogenesis. We ablated *Tbx5*$^{+}$*/Mef2cAHF*$^{+}$ precursors to determine the essential roles of the lineage-labeled compartment boundary for cardiac septation and chamber development. By leveraging a genetic lesion of the CHD gene *Tbx5*, our work uncovers the genetic regulation of the *Tbx5*$^{+}$*/Mef2cAHF*$^{+}$ lineage-labeled compartment boundary for proper IVS patterning. We deployed single-cell RNA sequencing (scRNA-seq) to discover TBX5-sensitive cues that are essential for compartment boundary regulation and formation of the IVS during heart development.

Results

Early cardiac progenitors for the IVS, IAS and AV complex regions

We used conditional dual-lineage labelling by *Tbx5*$^{CreERT2/+}$ or *Mef2cAHF-DreERT2* and marked cells during gastrulation at E6.5 with a single dose of tamoxifen-induced recombination. We followed separate reporter-labeled lineages by epifluorescence microscopy, histology or lightsheet microscopy (Fig. 1a–f). At E14.5, the *Tbx5*$^{+}$ lineage contributed to the left side of the IVS, often ending at a presumptive line marked at the apex by the IV groove, consistent with previous reports suggesting a lineage boundary[12,25,34]. The *Tbx5*$^{+}$ and *Mef2cAHF*$^{+}$ lineages showed largely complementary patterns, with notable overlap of *Tbx5*$^{+}$ and *Mef2cAHF*$^{+}$ lineages at the IVS, AV complex (AVco) region and interatrial septum (IAS) (Fig. 1b,d,f).

To better visualize the *Tbx5*$^{+}$*/Mef2cAHF*$^{+}$ lineage, we used a conditional intersectional-lineage labeling approach. Using a lineage reporter that is responsive to both CreERT2 and DreERT2 (ref. 35), we observed a spatial pattern of the *Tbx5*$^{+}$*/Mef2cAHF*$^{+}$ lineage in the IVS, AVco region and IAS (Fig. 1g). At E14.5, the septal lineage extended to the apex of the heart via the IVS and to the base of the heart at the AVco region, as well as to the IAS superiorly (Fig. 1h–j). These results expanded upon previous findings in the developing IVS at E10.5 (ref. 25), by identifying contributions from *Tbx5*$^{+}$*/Mef2cAHF*$^{+}$ progenitors to additional anatomic sites during chamber formation and septation. Moreover, lineage contributions to sites of chamber septation were derived from *Tbx5*$^{+}$*/Mef2cAHF*$^{+}$ progenitors at E6.5 (Extended Data Fig. 1a–c), but not later at E8.5 or E10.5, implicating a

https://doi.org/10.1038/s44161-025-00755-6

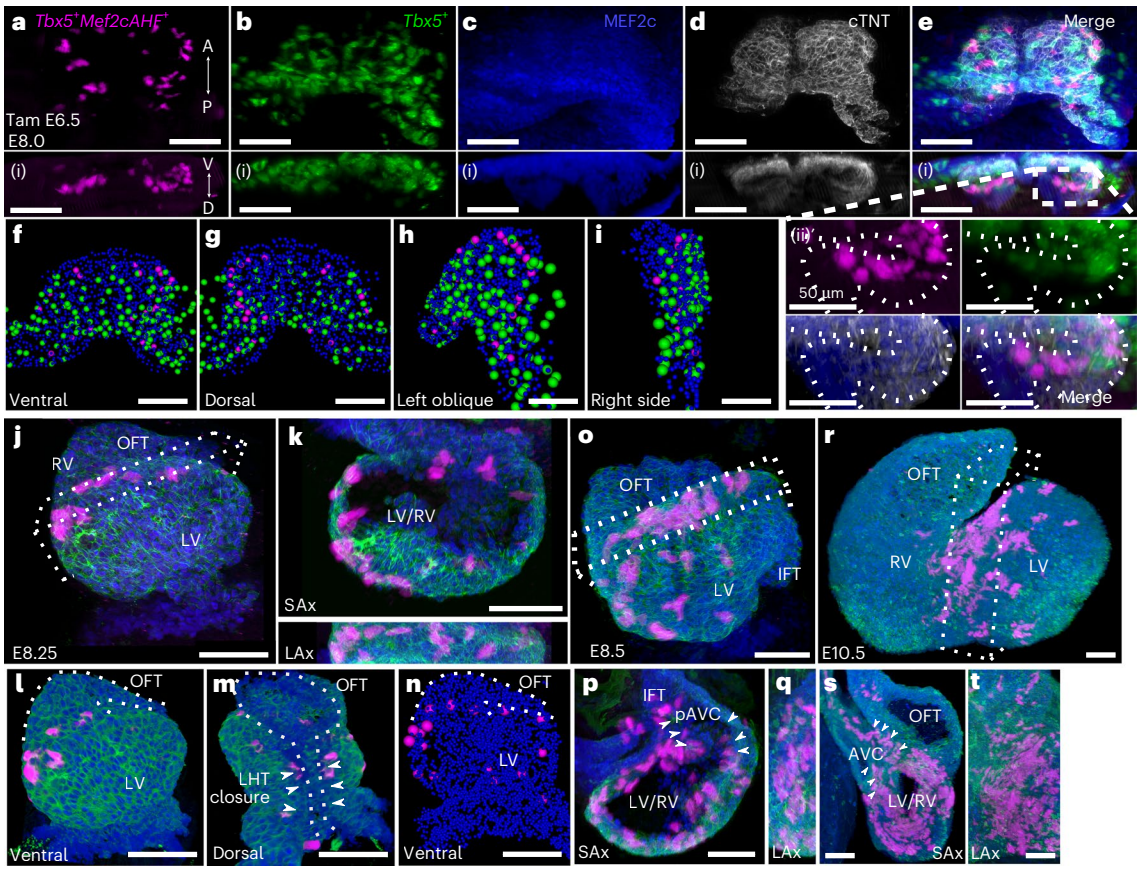

Fig. 2 | *Tbx5*$^+$*/Mef2cAHF*$^+$ lineage is prefigured in early mouse heart development. a–**i**, Frontal (**a**–**e**), transverse (**a**(i)–**e**(i)), magnified transverse (**e**(ii)) and cell segmentation views (**f**–**i**) of maximum Z-projections of whole-mount embryos by lightsheet imaging at E8.0 show the *Tbx5*$^+$ lineage (ZsGreen), and immunostaining of tdTomato for the *Tbx5*$^+$*/Mef2cAHF*$^+$ lineage, MEF2c and cTNT in *Tbx5*$^{CreERT2/+}$;*Mef2cAHF-DreERT2*;*ROSA26*$^{Ai6/Ai66}$ embryos. A↔P, anterior–posterior axis; V↔D, ventral–dorsal axis. At E8.0 (approximately three somites), *Tbx5*$^+$ lineage cells are restricted to a ventral domain, whereas *Tbx5*$^+$*/Mef2cAHF*$^+$ lineage cells originate along a boundary separating presumptive *Tbx5*$^+$ and *Tbx5*$^-$-lineage compartments. *Tbx5*$^+$*/Mef2cAHF*$^+$ lineage cells lie in an apparent planar ringlet in the dorsal–ventral axis that expands as the heart tube grows. **j**–**n**, At E8.25 (approximately six somites), with dorsal closure of the linear heart tube (LHT) underway, the *Tbx5*$^+$*/Mef2cAHF*$^+$ lineage cells form a ring situated between the RV and LV primordia, which is observed from multiple perspectives including the anterior, short-axis (SAx) and long-axis (LAx) views. **o**–**q**, At E8.5 (approximately nine somites), *Tbx5*$^+$*/Mef2cAHF*$^+$ lineage cells are observed in a portion of the AV canal primoridium (pAVC and arrowheads). IFT, inflow tract. **r**–**t**, At E10.5, a band of *Tbx5*$^+$*/Mef2cAHF*$^+$ lineage cells extends from the IV groove at the outer curvature to the inner curvature of the heart. SAx and LAx show that *Tbx5*$^+$*/Mef2cAHF*$^+$ lineage cells occupy a crossroads for heart morphogenesis, spanning the growing IVS to the AV canal (AVC), adjacent to the OFT. All scale bars, 100 µm.

narrow, early window for capturing *Tbx5*$^+$*/Mef2cAHF*$^+$ septal progenitors during cardiac mesoderm formation.

Tbx5$^+$*/Mef2cAHF*$^+$ septal lineage is prefigured in early mouse heart development

To characterize the lineage derived from *Tbx5*$^+$*/Mef2cAHF*$^+$ septal progenitors during early heart development, we examined the localization of the lineage before heart tube formation at E8.0 (Extended Data Fig. 1d–f, Fig. 2 and Video 1). By lightsheet imaging, the pattern of the *Tbx5*$^+$*/Mef2cAHF*$^+$ lineage was detected at the dorsal aspect of the *Tbx5*$^+$ lineage, at an interface between *Tbx5*$^+$ and *Tbx5*$^-$ lineage compartments (Fig. 2a–e(ii)). Cell segmentation at this early stage revealed that the *Tbx5*$^+$*/Mef2cAHF*$^+$ lineage resembled a nascent halo of cells that became readily apparent at later stages of heart development (Fig. 2f–i).

We further examined the lineage contributions of *Tbx5*$^+$*/Mef2cAHF*$^+$ septal progenitors at subsequent time points during cardiac morphogenesis. At the linear heart tube stage at E8.25, the labeled *Tbx5*$^+$*/Mef2cAHF*$^+$ lineage appeared intricately arranged into a ring of cells between the future left and right ventricles (Fig. 2j,k). This circlet configuration was maintained during rightward looping of the heart at E8.5 (Fig. 2o–q) and subsequent chamber formation. At E10.5, we observed a band of lineage-labeled cells from the IV groove at the outer curvature to the inner curvature near the AV groove that extended posteriorly to the atria (Fig. 2r–t), reminiscent of the 'primary ring'[9–11] and consistent with oriented cell growth of the developing IVS[12]. Optical sections showed the labeled lineage superiorly at the crossroads of the AV canal, OFT and atria (Fig. 2s). This populates a morphogenetic nexus, where VSDs can occur owing to abnormal connections between the IVS and the AV canal, OFT cushions or the muscular septum itself. In the atria, we noted lineage-labeled cells at the midline, superiorly and inferiorly (Supplementary Fig. 1a–e), consistent with clonal growth in the body of the atria[12]. This suggests that the *Tbx5*$^+$*/Mef2cAHF*$^+$ lineage potentially marks the presumptive location of the IAS for later stages. Consequently, these data are consistent with the notion that the *Tbx5*$^+$*/Mef2cAHF*$^+$ lineage is configured early in heart development, well before subsequent morphogenetic events of chamber formation and cardiac septation.

IVS disorganization and ventricular hypoplasia from cell ablation of *Tbx5*$^+$*/Mef2cAHF*$^+$ progenitors

To determine the role of the *Tbx5*$^+$*/Mef2cAHF*$^+$ septal progenitors during heart development, we conditionally ablated these cells at E6.5. To this end, we generated an intersectional recombinase-responsive

https://doi.org/10.1038/s44161-025-00755-6

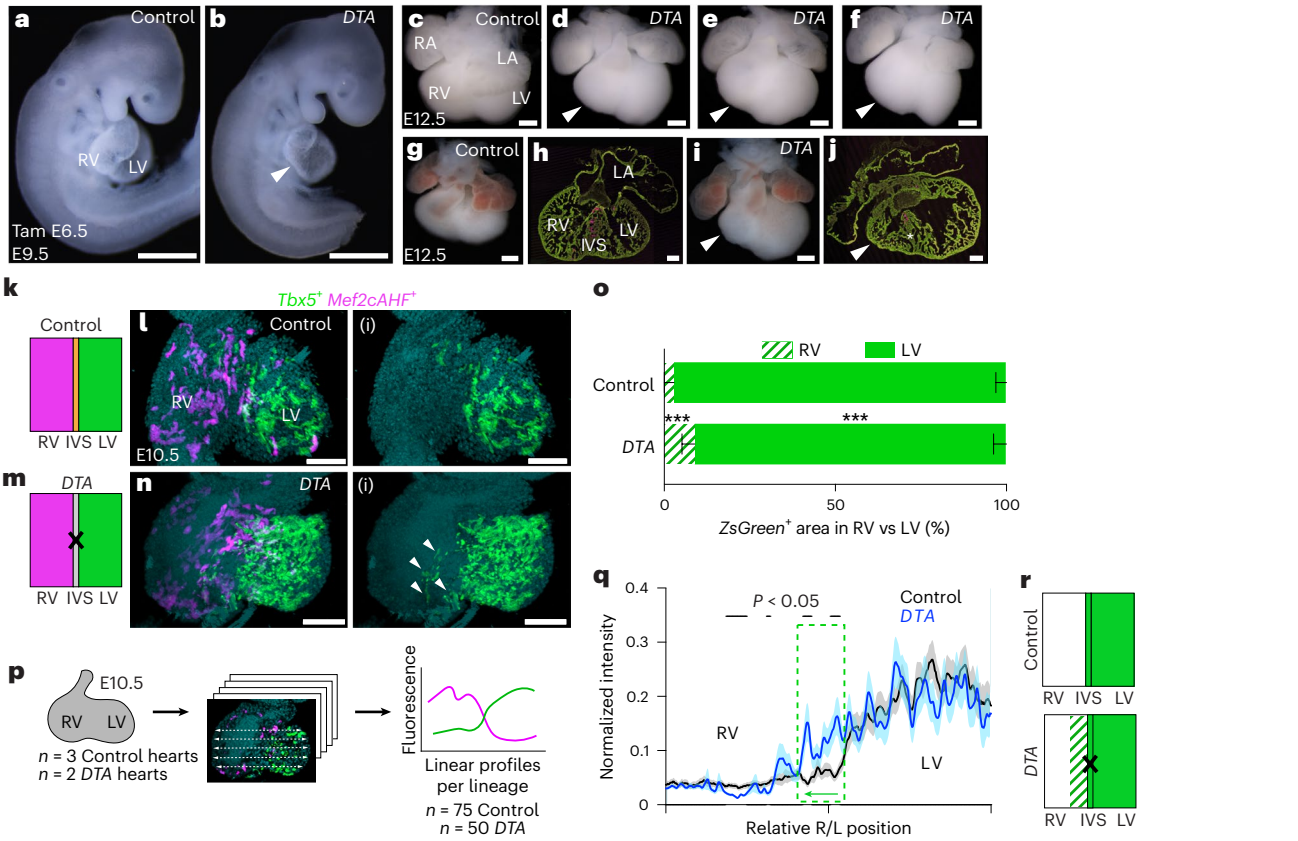

Fig. 3 | Cell ablation of *Tbx5*$^+$/*Mef2cAHF*$^+$ progenitors causes RV hypoplasia, IVS disorganization and lineage mixing. a–j, Misexpression of *diphtheria toxin* (*DTA*) in *Tbx5*$^+$/*Mef2cAHF*$^+$ progenitors in *Tbx5*$^{CreERT2/+}$;*Mef2cAHF-DreERT2*;*ROSA26*$^{Ai66/+}$;*Hip11*$^{intersectional\text{-}DTA/+}$ embryos (*DTA*), compared with *Tbx5*$^{CreERT2/+}$;*Mef2cAHF-DreERT2*;*ROSA26*$^{Ai66/+}$;*Hip11*$^{+/+}$ (control), resulted in RV hypoplasia (arrows) at E9.5 (**a** and **b**; scale bars, 500 µm) and E12.5 (**c**–**j**; scale bars, 250 µm (**c**–**g**, **i**), 150 µm (**h**), 100 µm (**j**)), along with disorganization and non-compaction of the IVS (asterisk) (**g**–**j**). **k**–**n**(i), At E10.5, mixing of the *Tbx5*$^+$ lineage (white arrows in **n**(i) show ectopic *Tbx5*$^+$ lineage ZsGreen cell in the right heart) was observed by lightsheet microscopy in *Tbx5*$^{CreERT2/+}$;*Mef2cAHF-DreERT2*;*ROSA26*$^{Ai6/Ai66b}$;*Hip11*$^{intersectional\text{-}DTA/+}$ embryos (*DTA*) ($n = 2$) compared with *Tbx5*$^{CreERT2/+}$;*Mef2cAHF-DreERT2*;*ROSA26*$^{Ai6/Ai66b}$;*Hip11*$^{+/+}$ embryos (control) ($n = 3$). Scale bars, 100 µm (**l**–**n**(i)). **k**,**m**, Cartoon depictions of the experiment. **o**, Distribution of the *Tbx5*$^+$ lineage by ventricular chamber shows that the *Tbx5*$^+$ lineage is increased in the RV of *DTA* mutants (***$P = 0.000513$ by two-sided *t*-test) compared with controls. Cells of the RV and LV were evaluated in five optical slices at different anterior–posterior planes per embryonic heart sample of three controls and two mutants. Mean and standard deviation are shown. **p**–**r**, Linear profiles quantified fluorescence intensity across the heart at the right or left (R/L) positions. *Tbx5*$^+$ lineage cells expanded rightward into the RV (depicted in **r** by the hashed area; the dashed green box in **q** shows significant difference between traces, indicative of a rightward expansion (green arrow)), consistent with a compartment boundary disruption. Linear profiles at five apical–basal planes per optical slice, for five optical slices at different anterior–posterior planes per embryonic heart sample of three controls and two *DTA* mutants were assessed, as depicted in **p**. Statistical significance ($P < 0.05$) between linear profiles of control and *DTA* mutants was determined by Welch's two-sided *t*-test at each position along the right–left axis. Mean and standard error of the mean are shown. Precise *P*values can be found in the source data.

DTA176 knock-in mouse allele at the *Hip11* safe-harbor locus, by which cells would be killed where approximately 100–200 molecules of DTA176 were expressed[36,37]. Following the administration of a single dose of tamoxifen to pregnant dams at E6.5, intersectional-*DTA* mutant (*Tbx5*$^{CreERT2/+}$;*Mef2cAHF-DreERT2*;*Hip11*$^{intersectional\text{-}DTA176/+}$) embryos showed RV hypoplasia (that is, a reduction in RV chamber size) at E9.5 (Fig. 3a,b) and E12.5 (Fig. 3c–j), together with IVS disorganization and non-compaction with a blunted IV groove (Fig. 3h,j). Furthermore, there were defects of the AVco region and absence of the IAS (Fig. 3h,j). A few *Tbx5*$^+$/*Mef2cAHF*$^+$ lineage cells remained in mutant embryos, probably reflecting some degree of inefficient dual recombination of both the reporter allele[38,39] and the intersectional-*DTA* transgene[40]. Beyond E12.5, intersectional-*DTA* mutant embryos were not recovered. Results of *Tbx5*$^+$/*Mef2cAHF*$^+$ progenitor ablation contrasted with findings after the ablation of the LV-enriched *Hand1*$^+$ lineage, which caused LV hypoplasia at E10.5 and full recovery of the LV by E16.5 (ref. 41). Hence, our findings suggested that the *Tbx5*$^+$/*Mef2cAHF*$^+$ septal progenitors were important not only for IVS development and AV septation, but also for RV chamber formation.

Lineage mixing from disruption of an IVS compartment boundary after ablation of *Tbx5*$^+$/*Mef2cAHF*$^+$ septal progenitors

We hypothesized that the *Tbx5*$^+$/*Mef2cAHF*$^+$ septal progenitors establish a compartment boundary at the IVS. Following the ablation of *Tbx5*$^+$/*Mef2cAHF*$^+$ septal progenitors, we predicted that if either lineage expanded into the other ventricular chamber, then this would suggest lineage mixing from loss of compartment boundary integrity. To determine whether *Tbx5*$^+$/*Mef2cAHF*$^+$ septal progenitors were essential for a compartment boundary at the IVS, we tested the effects of ablating *Tbx5*$^+$/*Mef2cAHF*$^+$ septal progenitors on lineage segregation (Fig. 3k–n(i)). We quantified the distribution of the *Mef2cAHF*$^+$ or *Tbx5*$^+$ lineages at E10.5 after administration of a single dose of tamoxifen at E6.5 using two metrics. First, we assessed each fluorescently labeled lineage by distribution in the RV or LV. We observed that cells of the *Mef2cAHF*$^+$ lineage were enriched in the RV of control embryos (*Tbx5*$^{CreERT2/+}$;*Mef2cAHF-DreERT2*;*Hip11*$^{+/+}$), and this distribution was not different in mutant intersectional-*DTA* embryos (*Tbx5*$^{CreERT2/+}$;*Mef2cAHF-DreERT2*;*Hip11*$^{Intersectional\text{-}DTA176/+}$) (Extended Data Fig. 2a–c).

Cells of the *Tbx5*$^+$ lineage were normally enriched in the LV and nearly absent in the RV of controls. However, in mutant intersectional-*DTA* embryos, a larger percentage of *Tbx5*$^+$ lineage cells were located in the RV (Fig. 3o).

Second, we quantified the fluorescence intensity as a linear profile across the ventricular chambers by lightsheet microscopy (Fig. 3p). Cells of the *Mef2cAHF*$^+$ lineage were again enriched in the RV in controls and showed reduced fluorescence in the LV in mutant intersectional-*DTA* embryos (Extended Data Fig. 2d–f). Moreover, cells of the *Tbx5*$^+$ lineage were again highly enriched in the LV and rarely found in the RV. By contrast, cells of the *Tbx5*$^+$ lineage in intersectional-*DTA* mutants were observed more rightward, including in the RV (Fig. 3q,r). Therefore, we inferred that *Tbx5*$^+$/*Mef2cAHF*$^+$ progenitors were essential for preventing lineage mixing between the RV and LV, by maintaining compartment boundary integrity at the developing IVS. These data may imply preferential regulation of first heart field derivatives over the adjacent second heart field derivatives.

Heterozygous loss of *Tbx5* in the IVS leads to VSDs

TBX5 is a transcription factor gene that causes VSDs in Holt–Oram syndrome from haploinsufficiency in humans[42–44] and mice[45]. We wondered whether heterozygous loss of *Tbx5* in the IVS would cause VSDs. We used the *Mef2cAHF-Cre*[46] in combination with a conditional deletion of *Tbx5* (*Tbx5*^{flox})[45], to conditionally delete *Tbx5* heterozygously in a domain that overlaps with *Tbx5* expression at the IVS[13]. We observed membranous VSDs in *Mef2cAHF-Cre;ROSA26*$^{mTmG/+}$*;Tbx5*$^{flox/+}$ mutant embryos (n = 4/7) compared with controls (n = 0/3), at E14.5 (Extended Data Fig. 3a–c). This provided evidence that appropriate *Tbx5* dosage in the IVS was essential for proper ventricular septation. Whether *Tbx5* is required in *Mef2cAHF*$^+$ progenitors or in a subsequent stage for IVS formation remains to be determined.

Disturbed septal lineage contributions from reduced *Tbx5*

As TBX5 dosage reduction globally or only in the IVS results in VSDs, we reasoned that reducing the TBX5 dosage may affect the regulation of the *Tbx5*$^+$/*Mef2cAHF*$^+$ septal progenitors and their subsequent lineage contributions. We evaluated a reduction of *Tbx5* using a hypomorphic (*Tbx5*^{CreERT2}) allele[44], which has been used thus far in this study to follow the *Tbx5*$^+$ and *Tbx5*$^+$/*Mef2cAHF*$^+$ lineages, in combination with a conditional deletion of *Tbx5* (*Tbx5*^{flox})[45] at E6.5. This resulted in levels of *Tbx5* that are estimated to be about 25% of the wild type in the *Tbx5*$^+$ lineage of *Tbx5* mutants. In control embryos (*Tbx5*$^{CreERT2/+}$*;Mef2cAHF-DreERT2;ROSA26*$^{Ai66/Ai6}$), the *Tbx5*$^+$/*Mef2cAHF*$^+$ septal lineage overlapped at the lineage front of the *Tbx5*$^+$ lineage in the IVS, from the base to the apex of the heart at the IV groove, spanning from anterior to posterior of the heart in the IVS (Fig. 4a–a(ii), Extended Data Fig. 4a,b and Video 2). Among *Tbx5*$^{CreERT2/flox}$ mutant embryos (*Tbx5*$^{CreERT2/flox}$*;Mef2cAHF-DreERT 2;ROSA26*$^{Ai66/Ai6}$), we found that reduced TBX5 dosage at E6.5 caused a spectrum of defects, frequently including VSDs, ASDs or AV canal defects at E14.5 (Fig. 4b–d(i)), reminiscent of features of Holt–Oram syndrome[42,43,47]. The normally organized distribution of the tdTomato$^+$ cells was highly irregular in the *Tbx5*$^{CreERT2/flox}$ mutant hearts regardless of VSDs (Extended Data Fig. 4a–h). tdTomato$^+$ cells were less apparent in the posterior IVS (Fig. 4a(i),a(ii),b(i),b(ii),c(i),c(ii),d(i)) and IAS (Supplementary Fig. 2), and tdTomato$^+$ cells were nearly absent in a heart that showed a severe AV canal defect and chamber hypoplasia (Fig. 4d,d(i) and Extended Data Fig. 4g,h).

We used quantitative morphometry to assess the position and distribution of the *Tbx5*$^+$/*Mef2cAHF*$^+$ septal lineage at the IVS. We tested this by quantifying linear profiles of the labeled *Tbx5*$^+$/*Mef2cAHF*$^+$ septal lineage in the heart. We found that both distribution and position of the *Tbx5*$^+$/*Mef2cAHF*$^+$ septal lineage were disturbed in *Tbx5*$^{CreERT2/flox}$ mutants (Fig. 4e–h and Extended Data Fig. 4i–k), including an increase of tdTomato$^+$ cells leftward in the LV, suggesting abnormal lineage position. As well, we observed a broader band of *Tbx5*$^+$/*Mef2cAHF*$^+$ septal lineage cells (Fig. 4g,h), suggesting that the proper TBX5 dosage maintains the integrity of the compartment boundary marked by the *Tbx5*$^+$/*Mef2cAHF*$^+$ lineage at the IVS. We also observed a reduction, or sometimes absence, of the labeled septal lineage among AVco region cells, as well as remnant atrial septal tissue in *Tbx5*$^{CreERT2/flox}$ mutants (Fig. 4d,d(i)).

We further observed that cells of the *Tbx5*$^+$/*Mef2cAHF*$^+$ lineage in the IVS were arranged like a stack of coins, especially from the apex to the mid-septum (Fig. 4a(ii)). We wondered whether the proper TBX5 dosage might be necessary for maintaining appropriate cell arrangement in the IVS. Therefore, cell alignment was determined and quantified by two metrics, average orientation score or directional coherency. In *Tbx5*$^{CreERT2/flox}$ mutant hearts, *Tbx5*$^+$/*Mef2cAHF*$^+$ lineage (tdTomato$^+$) and *Tbx5*$^+$ lineage (ZsGreen$^+$) cells were reduced in the dominant direction of cell orientation and were more frequently in the orientation orthogonal to the dominant direction (Fig. 4i–t and Extended Data Fig. 4l–s). Furthermore, both lineages showed worse directional coherency in *Tbx5*$^{CreERT2/flox}$ mutants (Fig. 4t and Extended Data Fig. 4u). In a complementary analysis, we also evaluated the cell geometry and tissue architecture of the IVS using staining for cell borders by wheat germ agglutinin (WGA) and nuclei by 4′,6-diamidino-2-phenylindole (DAPI) staining. We found in IVS cardiomyocytes of *Tbx5* mutants that the cell diameter and area were enlarged (Fig. 4u–x and Supplementary Fig. 3a–h(i)), while cell eccentricity (a measure of a cell's elongation) and nuclei density were reduced (Fig. 4y,z). Taken together, this evidence supports the notion that TBX5 is important for proper cell arrangement in the IVS.

Tbx5-sensitive genes encode guidance cues

To find downstream effectors of Tbx5 that may mediate the regulation of *Tbx5*$^+$/*Mef2cAHF*$^+$ lineage cells, we applied scRNA-seq at E13.5, before completion of ventricular septation. We microdissected the RV, LV and IVS + AVco regions in controls and *Tbx5* mutants (*Tbx5*$^{CreERT2/flox}$*;Mef2cAHF-DreERT2;ROSA26*$^{Ai66/Ai6}$) (Fig. 5a). These samples were labeled at E6.5 for progenitors of the *Tbx5*$^+$/*Mef2cAHF*$^+$ lineage (*tdTomato*$^+$) and *Tbx5*$^+$ lineage (*ZsGreen*$^+$). In samples from each cardiac tissue region, we detected clusters enriched for *Tnnt2*$^+$ cardiomyocytes (CMs), *Postn*$^+$ fibroblasts, *Plvap*$^+$ endothelial cells, *Tbx18*$^+$/*Wt1*$^+$ epicardial cells, *Hba-x*$^+$ red blood cells and *C1qb*$^+$ white blood cells (Fig. 5b and Extended Data Fig. 5a–i).

In particular, *tdTomato*$^+$ cells were most abundant among clusters of *Tnnt2*$^+$ CMs of the IVS + AVco regions (Fig. 5c). However, we were unable to identify a gene expression signature that was unique to the *Tbx5*$^+$/*Mef2cAHF*$^+$ lineage, beyond the lineage marker itself, at this stage. Likewise, *ZsGreen*$^+$ cells were also enriched among clusters of *Tnnt2*$^+$ CMs in this region (Fig. 5d), indicative of the *Tbx5*$^+$ lineage contribution to CMs in the region, as well as a site of conditional reduction of *Tbx5* among *Tbx5* mutants.

We then focused our analysis on a subset of *Tnnt2*$^+$ enriched clusters from IVS + AVco regions. We identified genotype-enriched clusters that were abundant with cells from controls (cluster 5) or *Tbx5* mutants (cluster 10) (Fig. 5e,f). In the mutant-enriched cluster 10, genes typically expressed in ventricular trabeculae were enriched (Fig. 5g,h). These included natriuretic peptide *Nppa*, transcription factor *Cited1* and bone morphogenetic protein *Bmp10*, suggesting ectopic expression of these trabecular genes in the IVS of *Tbx5* mutants. Intriguingly, guidance cues *Netrin1* (*Ntn1*) and *Slit2*, which are best known for axonal development or vasculogenesis[48], were also dysregulated (Fig. 5g,h, Extended Data Fig. 5j,k and Supplementary Fig. 4a,b). Notably, *SLIT2* is implicated as a CHD-risk gene in mice and humans[49–52]. For *NTN1*, it's link to human CHD requires further clarification, as a copy number variation by intragenic deletion of *NTN1*, along with heterozygous loss of 22q11.21 and gain of the Y chromosome, was associated with septal defects in a patient[53]. Control-enriched cluster 5 included genes expressed in the AVco region, encoding the Wnt co-receptor *Rspo3*,

https://doi.org/10.1038/s44161-025-00755-6

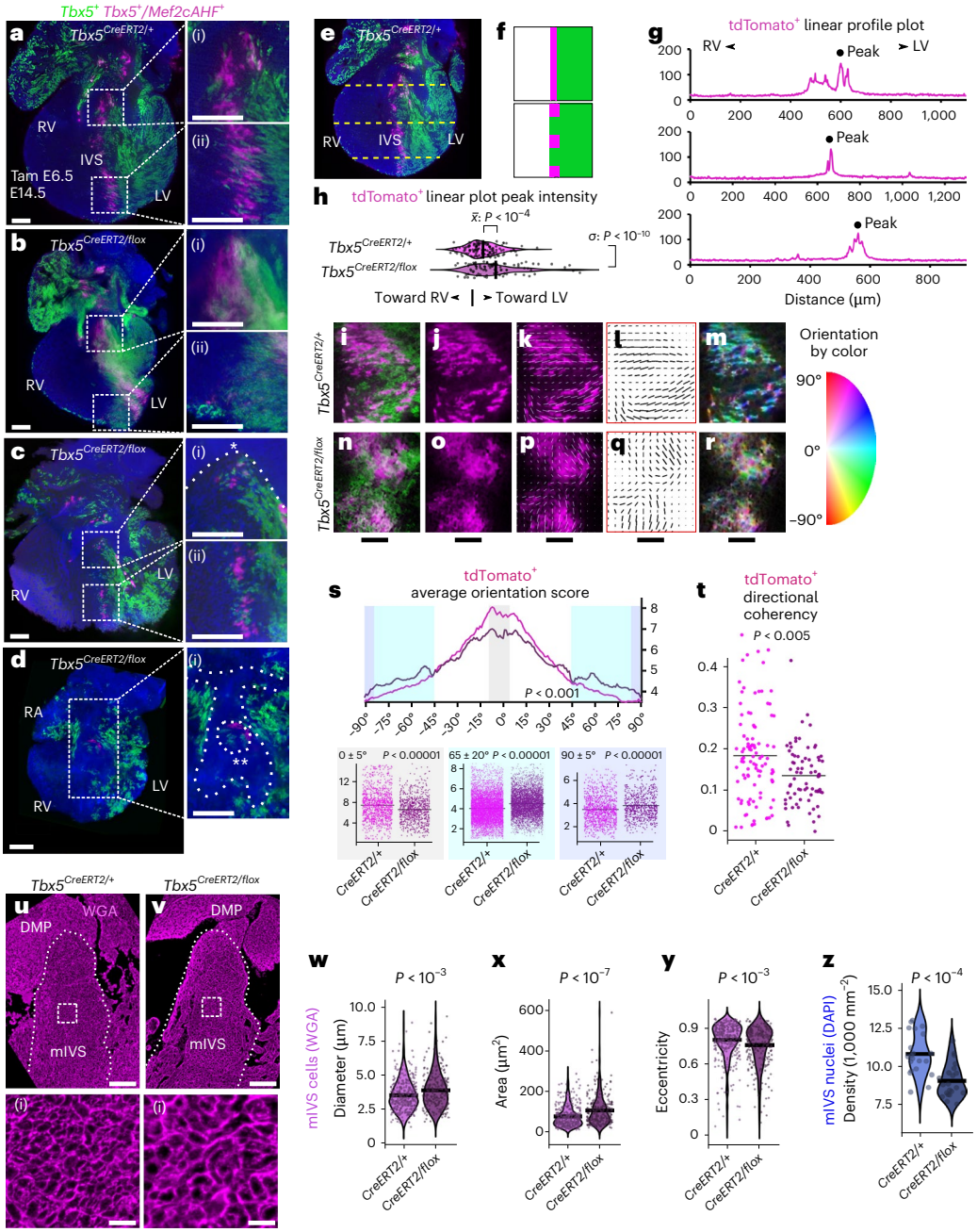

Fig. 4 | Reduced TBX5 dosage caused VSDs, perturbations to IVS boundary position and integrity, and abnormal IVS cell arrangement. **a**, Mid-posterior optical sections from lightsheet microscopy of a control (*Tbx5*$^{CreERT2/+}$;*Mef2cAHF-DreERT2*;*ROSA26*$^{Ai6/Ai66}$) heart show *Tbx5*$^{+}$ lineage (ZsGreen) and *Tbx5*$^{+}$/*Mef2cAHF*$^{+}$ lineage (tdTomato immunostaining) cells. *Tbx5*$^{+}$/*Mef2cAHF*$^{+}$ lineage cells in the IVS extended from the base (**a**(i)) to the apex (**a**(ii)) of the heart, where cells were highly organized. **b**–**d**, A spectrum of phenotypes of *Tbx5*$^{CreERT2/flox}$ mutants (*Tbx5*$^{CreERT2/flox}$;*Mef2cAHF-DreERT2*;*ROSA26*$^{Ai6/Ai66}$) were observed, including intact IVS (**b**–**b**(ii)), membranous VSD (**c**–**c**(ii), asterisk) and AV septal defect (double asterisk in **d**(i)). **b**(i),**b**(ii),**c**(i),**c**(ii),**d**(i), A maldistribution and disorientation of *Tbx5*$^{+}$/*Mef2cAHF*$^{+}$ lineage cells were observed in *Tbx5*$^{CreERT2/flox}$ mutants. **a**–**d**(i), Scale bars, 200 μm. **e**–**h**, Linear plot profiles at positions along the anterior–posterior and apical–middle–basal axis (dashed lines) of control (116 profiles from 4 samples) and *Tbx5*$^{CreERT2/flox}$ mutant (87 profiles from 3 samples) hearts for *Tbx5*$^{+}$/*Mef2cAHF*$^{+}$ lineage cells showed a leftward shift of boundary positioning and broadening of the *Tbx5*$^{+}$/*Mef2cAHF*$^{+}$ lineage position, consistent with lineage mixing. The image in **e** is a repeat of the image in **a**. **f**, Cartoon depiction. **g**,Examples of linear profile plots are shown, and aggregated data are depicted and quantified (**h**). Statistics determined by two-sided unpaired *F*-test to compare variance ($P = 2.621 \times 10^{-11}$) and two-sided unpaired *t*-test ($P = 9.741 \times 10^{-5}$) to compare means. **i**–**s**, Orientation scores for cells from each channel (tdTomato^{+} or ZsGreen^{+}) were delineated for each genotype, and distributions were plotted as a function of angle. *Tbx5*$^{CreERT2/flox}$ mutant hearts scored worse for orientation of *Tbx5*$^{+}$/*Mef2cAHF*$^{+}$ lineage (tdTomato^{+}) cells in the dominant direction (range from −5° to 5°) and scored higher in the orientation orthogonal to the dominant direction (range from 85° to 95° and −85° to −95°), as determined in **s** by two-sided Watson U2 test across all orientations ($P < 0.001$) or by two-sided Wilcoxon rank sum test with continuity correction for selected orientations ($P = 3.207 \times 10^{-10}$, 2.2×10^{-16}, 7.839×10^{-9}, for left-to-right plots). **i**–**r**, Scale bars, 100 μm. **t**, *Tbx5*$^{+}$/*Mef2cAHF*$^{+}$ lineage (tdTomato^{+}) cells showed worse directional coherency scoring in *Tbx5*$^{CreERT2/flox}$ mutants (99 regions from 4 controls, 74 regions from 3 mutants) by two-sided Wilcoxon rank sum test with continuity correction ($P = 0.003845$). **u**–**y**, Cell morphometry at E14.5 by WGA staining of cell membranes in the muscular IVS (mIVS) (dashed outline) of controls (3 planes per sample, 2 samples) and *Tbx5* mutants (3 planes per sample, 2 samples). Scale bars, 100 μm (**u**, **v**), 15 μm (**u**(i), **v**(i)). Images of **u**–**v**(i)) are repeated in Supplementary Data Fig. 3b,b(i),f,f(i). Quantification of cell diameter (**w**), area (**x**) and eccentricity (**y**). **z**, Nuclei density shown using DAPI staining of the IVS. Statistics were determined by two-sided unpaired *t*-tests (**w**: $P = 0.0002955$, **x**: $P = 2.9 \times 10^{-8}$, **y**: $P = 0.0007001$, **z**: $P = 5.296 \times 10^{-5}$).

https://doi.org/10.1038/s44161-025-00755-6

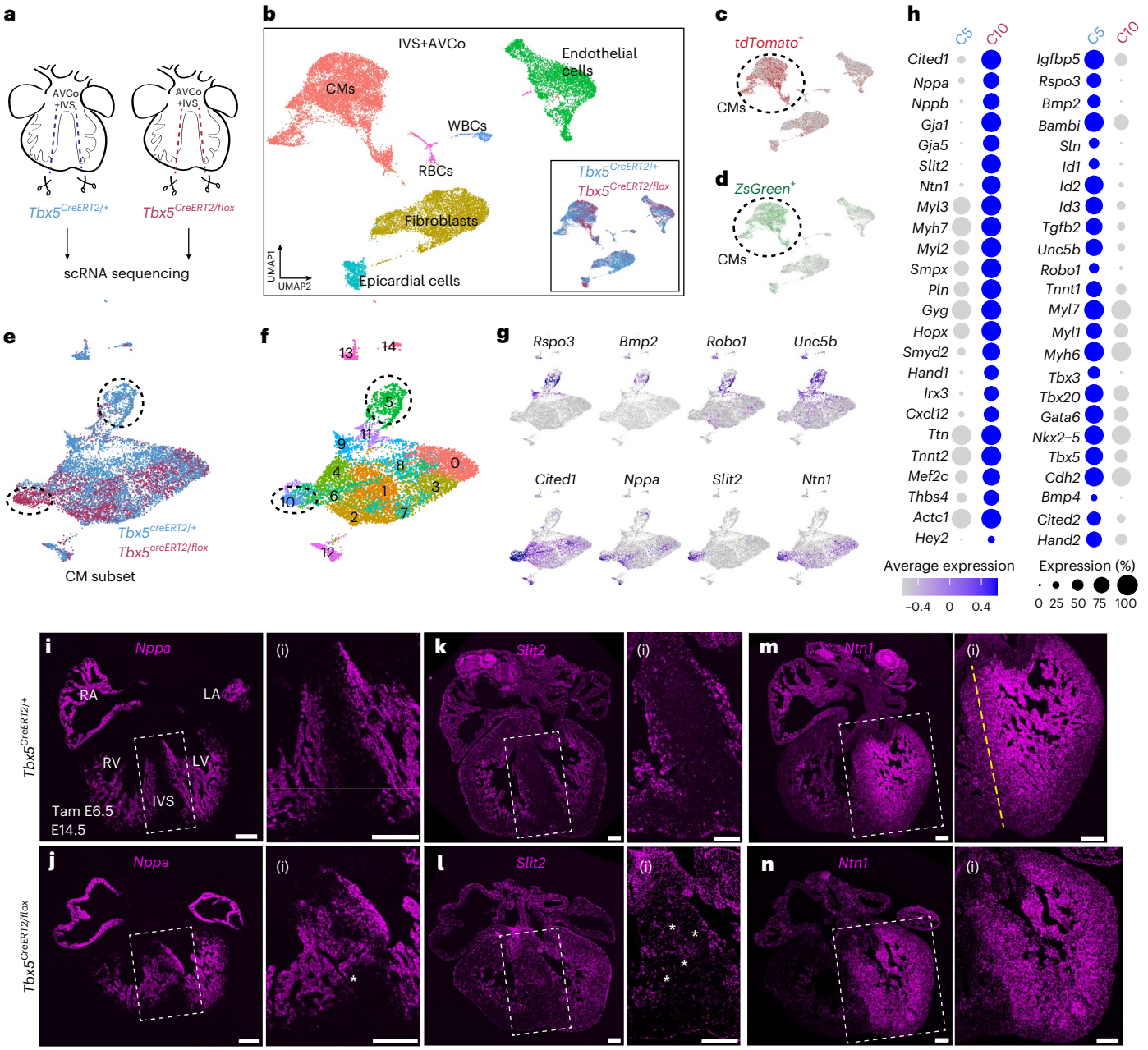

Fig. 5 | *Slit2* and *Ntn1* are *Tbx5*-sensitive genes in the IVS. a, At E13.5, we microdissected the RV, LV and IVS + AVCo regions in *Tbx5*$^{CreERT2/+}$ controls and *Tbx5*$^{CreERT/flox}$ mutants (*Tbx5*$^{CreERT2/flox}$;*Mef2cAHF-DreERT2*;*ROSA26*$^{Ai6/Ai66}$) with the labeled *Tbx5*$^{+}$/*Mef2cAHF*$^{+}$ lineage (*tdTomato*$^{+}$) and *Tbx5*$^{+}$ lineage (*ZsGreen*$^{+}$) cells, after a single dose of tamoxifen at E6.5. **b**, UMAP visualization of IVS + AVCo by cell type clusters and *Tbx5* genotype (inset) (controls, $n = 4$; *Tbx5* mutants, $n = 2$). WBCs, white blood cells; RBCs, red blood cells. **c**,**d**, *tdTomato*$^{+}$ (**c**) and *ZsGreen*$^{+}$ (**d**) cells are enriched among CMs. **e**,**f**, UMAP shows a *Tnnt2*$^{+}$ CM subset by *Tbx5* genotype (**e**) or Louvain clusters (**f**). **g**, Feature plots show that AVCo region genes (*Rspo3*, *Bmp2*, *Robo1*, *Unc5b*) are enriched among control-enriched cluster 5, suggesting downregulation of these genes in *Tbx5* mutants. Trabecular genes (*Cited1*, *Nppa*, *Slit2*, *Ntn1*) were enriched in the *Tbx5* mutant-enriched cluster 10. **h**, Dot plots of selected genes that are upregulated in cluster 10 (C10) or in cluster 5 (C5). The significance of adjusted $P < 0.05$ was determined by two-sided Wilcoxon rank sum. **i**–**n**, Fluorescence in situ hybridization of trabecular genes *Nppa*, *Slit2* and *Ntn1* in *Tbx5*$^{CreERT2/+}$ controls or *Tbx5*$^{CreERT2/flox}$ mutants at E14.5. **i**,**i**(i),**k**,**k**(i), *Nppa* and *Slit2* are normally expressed in the ventricular trabecular layer and excluded from the core of the IVS. **j**,**j**(i),**l**,**l**(i), In a *Tbx5*$^{CreERT2/flox}$ mutant with an intact IVS, *Nppa* and *Slit2* are misexpressed in the IVS (asterisks). **m**,**m**(i), *Ntn1* is normally expressed in the trabecular layer and in a gradient across the IVS from left to right, demarcated by a yellow dashed line. **n**,**n**(i), In a *Tbx5*$^{CreERT2/flox}$ mutant with an intact IVS, *Ntn1* is expanded across the IVS, flattening its gradient. All scale bars, 200 µm.

morphogen *Bmp2* and transcription factors *Tbx2* and *Tbx3*, and *Cdh2*, which encodes N-cadherin, suggesting that these genes are reduced in *Tbx5* mutants (Fig. 5g,h). As well, the SLIT receptor *Robo1*, which is implicated in mouse and human VSDs[49,51,54], and Netrin-receptor *Unc5b*, were also downregulated in *Tbx5* mutant cells (Fig. 5g,h).

We examined differential gene expression between controls or *Tbx5* mutants in *tdTomato*$^{+}$ (*Tbx5*$^{+}$/*Mef2cAHF*$^{+}$ septal lineage) or *ZsGreen*$^{+}$ (*Tbx5*$^{+}$ lineage) CMs. We found many differentially expressed genes that overlapped among comparisons of *tdTomato*$^{+}$ or *ZsGreen*$^{+}$ clusters, including *Nppa*, *Cited1* and *Slit2*, consistent with findings from cluster-to-cluster comparisons (Extended Data Fig. 5j,k).

We used orthogonal assays to validate candidate TBX5-sensitive genes. By fluorescence in situ hybridization in formalin-fixed paraffin-embedded sections, we observed a reduction of gene

expression of *Bmp2*, *Robo1 and Unc5b* in the AVco region of mutant hearts when compared with controls. (Extended Data Fig. 6a–f″). We found that the IVS-enriched gene *Irx2* was reduced in the IVS of *Tbx5* mutants (Extended Data Fig. 6g,h′). As well, we detected expansion of *Nppa* and *Slit2* into the IVS and compact layer of *Tbx5* mutant hearts, both of which are normally expressed only in the trabecular regions of both ventricles of control hearts (Fig. 5i–l(i)). Moreover, we discovered *Ntn1* expression enriched in LV trabecular CMs and in a gradient across the control IVS (Fig. 5m,m(i) and Extended Data Fig. 6m–m(ii)), consistent with immunostaining of NTN1 in the heart at E14.5 (Extended Data Fig. 6o). However, in *Tbx5* mutants, the *Ntn1* gradient was flattened and expanded in the IVS with reduced TBX5 dosage (Fig. 5n,n(i)). Interestingly, we observed abnormal *Nppa*, *Slit2* and *Ntn1* in *Tbx5* mutants with or without VSDs, suggesting that this dysregulated gene expression was not secondary to VSDs (Extended Data Fig. 6i–n″). Notably, earlier at E11.5, *Ntn1* was LV enriched during normal ventricular septation and broadly expanded into the RV of *Tbx5* mutants, while *Slit2* appeared unchanged in *Tbx5* mutants (Extended Data Fig. 7a–h). In addition, analysis of chromatin immunoprecipitation followed by sequencing (ChIP-seq) of TBX5 from embryonic mouse hearts[55] showed TBX5 occupancy at promoters of *Nppa*, *Slit2* and *Ntn1* (Extended Data Fig. 8a–c), suggesting that these guidance genes are likely to be direct targets of TBX5 in the heart.

Tbx5–*Slit2* and *Tbx5*–*Ntn1* genetic interactions

We evaluated whether genetic interactions existed between *Tbx5* and *Slit2* or *Ntn1* (Extended Data Fig. 9). As *Tbx5* heterozygous mutant ($Tbx5^{del/+}$)[45] mouse embryos show muscular or membranous VSDs, we wondered whether heterozygous *Slit2* or *Ntn1* loss-of-function (LOF) mutant embryos might alter *Tbx5*-dependent phenotypes. We mated $Tbx5^{del/+}$ mice with either *Slit2* ($Slit2^{+/-}$) or *Ntn1* ($Ntn1^{beta\text{-}actin\text{-}Cre/+}$ referred here subsequently as $Ntn1^{+/-}$ (refs. 56,57) heterozygous LOF mice. In $Tbx5^{del/+}$ embryos at E14.5, we observed membranous ($n = 5/8$) or muscular ($n = 3/8$) VSDs by histology (Extended Data Fig. 9a,b,e), consistent with previous reports[45]. Among $Slit2^{+/-}$ embryos at E14.5, we observed a membranous VSD ($n = 1/8$) (Extended Data Fig. 9c,e). This contrasted with a previous report that did not detect any VSDs in $Slit2^{+/-}$ albeit using a different mutant *Slit2* allele[49]. In $Tbx5^{del/+}$;$Slit2^{+/-}$ compound heterozygous embryos, we observed a non-significant effect on the reduction of membranous VSDs ($n = 5/8$) (log(odds ratio (OR)) = −2.5; $P = 0.09$ in a generalized linear model without adjustments for multiple comparisons) (Extended Data Fig. 9d,e), relative to the expected incidence of membranous VSDs if there was no genetic interaction between *Tbx5* and *Slit2*.

We next tested whether there was a genetic interaction between *Tbx5* and *Ntn1* (Extended Data Fig. 9f–j). In $Ntn1^{+/-}$ embryos, we observed a membranous ($n = 1/9$) or a muscular ($n = 1/9$) VSD. In $Tbx5^{del/+}$;$Ntn1^{+/-}$ compound heterozygous embryos, we observed a significant decrease of membranous VSDs ($n = 1/8$; log(OR) = −5.3; $P = 1 \times 10^{-3}$ by a generalized linear model without adjustments for multiple comparisons), relative to the expected incidence of membranous VSDs if there was no genetic interaction between *Tbx5* and *Ntn1*, but not significant changes to prevalence of muscular VSDs ($n = 4/8$; log(OR) = 0.12; $P = 0.93$), consistent with a genetic interaction between *Tbx5* and *Ntn1* for ventricular septation.

We wondered whether there were other quantitative histologic differences, in addition to the changes in incidence of VSD types. To quantify morphometry from histology, we leveraged a deep learning algorithm, known as CODA[58], to detect embryonic mouse heart components from hematoxylin and eosin sections. We generated three-dimensional (3-D) tissue reconstructions, to visualize and quantify anatomic structures and CHDs, including membranous and muscular VSDs, at cellular resolution (Fig. 6a–e). Using this machine learning method, we discovered that the cell density of the IVS, which we termed IVS fill, was increased in $Tbx5^{del/+}$; $Ntn1^{+/-}$ embryos compared with the wild type ($P < 0.05$ by Fisher's exact test), while classification of the IVS as trabecular was significantly reduced in $Tbx5^{del/+}$;$Ntn1^{+/-}$ embryos ($P < 0.05$ by Fisher's exact test) (Extended Data Fig. 9m). In addition, we estimated the minimal area for each membranous or muscular VSD, when present (Extended Data Fig. 9o,p). In $Tbx5^{del/+}$;$Slit2^{+/-}$ compound mutants, we detected statistically significant levocardia ($P < 0.001$ by Fisher's exact test), as determined by the axis of the heart compared with the spine and sternum (Extended Data Fig. 9q). This uncovered a genetic interaction between *Tbx5* and *Slit2* related to heart position, showing that machine learning-based morphometry can quantify unexpected anatomic findings.

Slit2 and *Ntn1* are essential for ventricular septation

To determine whether *Slit2* or *Ntn1* is essential for ventricular septation, we evaluated homozygous LOF mouse mutants for *Slit2* or *Ntn1* for VSDs. In $Slit2^{-/-}$ embryos at E14.5, we observed that homozygous loss of *Slit2* showed complete penetrance for VSDs, including membranous ($n = 3/4$; log(OR) = 5.0, $P = 0.02$ by a generalized linear model) or muscular VSD ($n = 1/4$) (Fig. 6f–i). We detected a statistically significant non-compacted IVS, which was determined by reduced IVS fill, and thinning of the right ventricular compact layer, and we quantified the area of membranous VSDs (Extended Data Fig. 10e–k). In addition, *Slit2* heterozygous LOF showed an increase of membranous VSDs ($n = 1/8$, OR = 2.5, $P = 0.02$ by a generalized linear model), relative to the expected incidence of membranous VSDs in controls. This showed a far higher incidence of VSDs in *Slit2* mutants than reported using an alternative *Slit2* LOF allele[49].

Fig. 6 | *Slit2* and *Ntn1* are essential for proper ventricular septation and compartment boundary regulation. a–**e**, Machine learning-based 3-D reconstructions of the embryonic heart and other tissues from histology at E14.5 were used for quantitative morphometric analysis of the embryonic heart (Extended Data Figs. 9 and 10). Compact myo, compact myocardium. **d**,**e**, A 3-D reconstruction of a membranous VSD (**d**) anteriorly and muscular VSD (**e**) posteriorly from a $Tbx5^{del/+}$ mutant heart. **f**–**i**, Histology (**f**–**h**) and incidence (**i**) of muscular or membranous (arrowhead) VSDs of *Slit2* mutants are shown. Membranous VSDs were enriched in $Slit2^{-/-}$ ($n = 3/4$, log(OR) = 5.0, $P = 0.02$ by a generalized linear model without adjustments for multiple comparisons) and $Slit2^{+/-}$ ($n = 1/8$, OR = 2.5, $P = 0.02$). The asterisk demarcates non-compacted IVS. **j**–**m**, Histology (**j**–**l**) and incidence (**m**) of muscular or membranous VSDs of *Ntn1* mutants are shown. Membranous VSDs were enriched in $Ntn1^{-/-}$ ($n = 6/7$, log(OR) = 6.32, $P = 0.0052$ by a generalized linear model without adjustments for multiple comparisons) and $Ntn1^{+/-}$ ($n = 1/9$, OR = 3.17, $P = 0.0052$ by a generalized linear model without adjustments for multiple comparisons). **n**–**r**, Lightsheet imaging of $Slit2^{-/-}$ mutant ($Tbx5^{CreERT2/+}$;*Mef2cAHF-DreERT2*;$ROSA26^{Ai66/+}$;$Slit2^{-/-}$) ($n = 4$) hearts at E14.5 showed a broadened distribution of the $Tbx5^{+}$/$Mef2cAHF^{+}$ lineage (tdTomato^{+} immunostaining) compared with controls ($Tbx5^{CreERT2/+}$;*Mef2cAHF-DreERT2*;$ROSA26^{Ai66/+}$;$Slit2^{+/+}$) ($n = 2$) (**n**–**q**), as quantified by linear profiles of fluorescence signals (**r**). Gray shading represents the control signal, and blue represents the mutant signal. The significance of $P < 0.05$ was determined by Welch's two-sided *t*-test at each position along the right–left axis. **s**–**v**, Lightsheet imaging of $Ntn1^{-/-}$ mutant ($Tbx5^{CreERT2/+}$;*Mef2cAHF-DreERT2*;$ROSA26^{Ai66/+}$;$Ntn1^{-/-}$) ($n = 6$) hearts at E14.5 showed a leftward shift in positioning of the $Tbx5^{+}$/$Mef2cAHF^{+}$ lineage compared with controls ($Tbx5^{CreERT2/+}$;*Mef2cAHF-DreERT2*;$ROSA26^{Ai66/+}$;$Ntn1^{+/+}$) ($n = 4$) (**s**–**u**), as quantified by linear profiles (**v**). The significance of $P < 0.05$ was determined by Welch's two-sided *t*-test at each position along the right–left axis. Precise *P* values are available in source data. **n**,**s**, Cartoon depictions. Panels **o**(i), **p**(i), **t**(i) and **u**(i) are optical sections that are orthogonal views to **o**, **p**, **t** and **u**. **q**, For each sample, three linear profiles (basal, middle, apical) spanned the ventricular chambers from right to left from optical sections every 50 µm from anterior to posterior of the heart. Precise values of statistics for **r** and **v** can be found in source data. **w**, Cartoon depicting the summary of findings. Scale bars, 500 µm (**a**, **o**–**u**(i)), 200 µm (**d**–**l**). Panel **w** created with BioRender.com.

https://doi.org/10.1038/s44161-025-00755-6

Ntn1 homozygous LOF embryos showed an increase of membranous VSDs ($n = 6/7$; log(OR) = 6.32, $P = 0.0052$ by a generalized linear model without adjustments for multiple comparisons) (Fig. 6f–m and Extended Data Fig. 10a–d) that we quantified by area, while other morphometry parameters were not significant (Extended Data Fig. 10l–r). *Ntn1* heterozygous LOF embryos were enriched for membranous VSDs ($n = 1/9$, OR = 3.17, $P = 0.0052$ by a generalized linear model), relative to the expected incidence of membranous VSDs in controls (Fig. 6m). Collectively, this morphologic evidence implicates *Slit2* and *Ntn1* in proper ventricular septation during heart development.

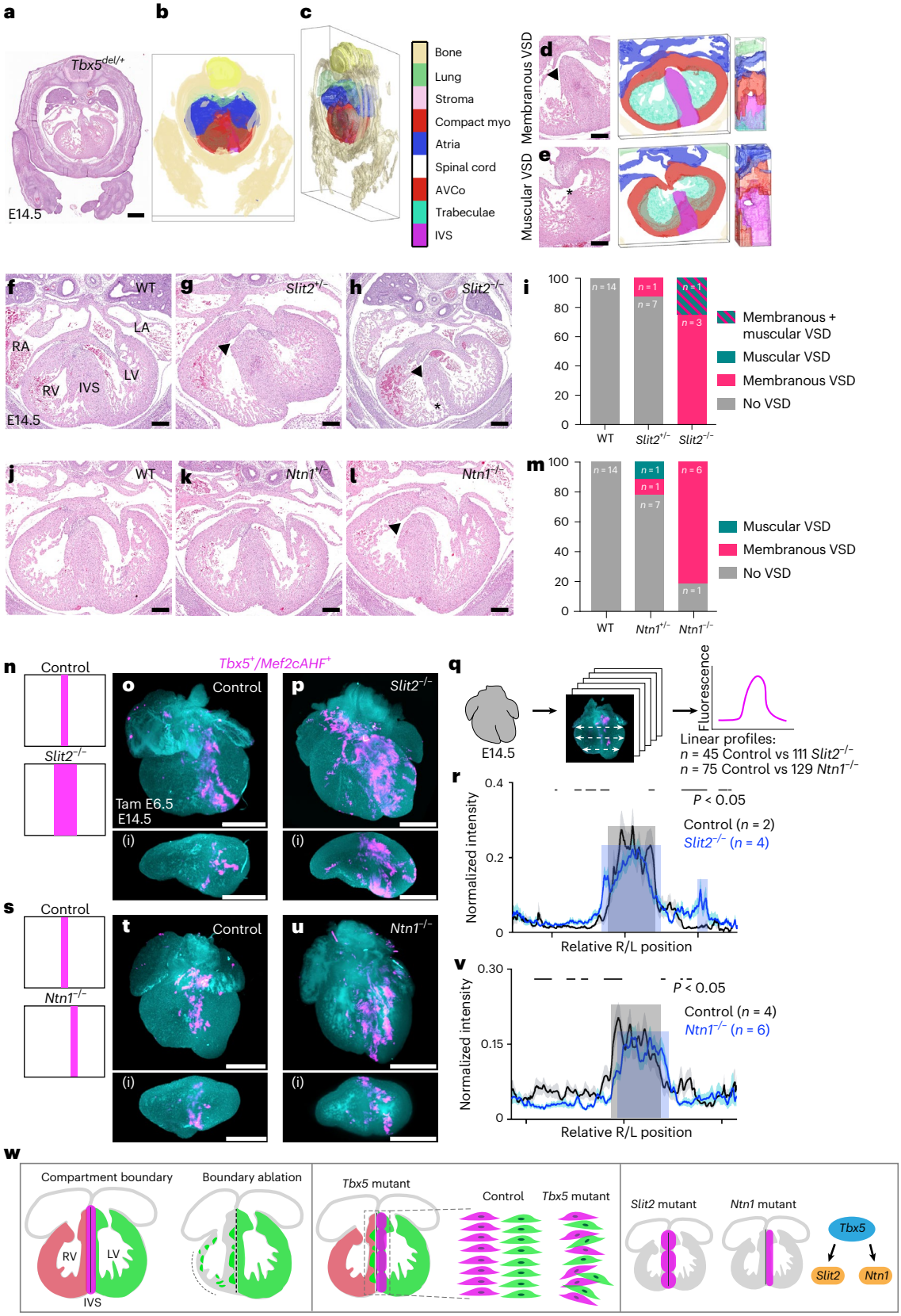

As *Slit2* and *Ntn1* were necessary for ventricular septation, we asked whether the loss of *Slit2* or *Ntn1* might disturb the distribution of the *Tbx5*$^{+}$/*Mef2cAHF*$^{+}$ lineage in the IVS. In homozygous *Slit2* LOF mutants with the lineage reporter (*Tbx5*$^{CreERT2/+}$;*Mef2cAHF-DreERT2*;*ROSA26*$^{Ai66/+}$;*Slit2*$^{-/-}$), we observed a statistically significant broadened distribution of the *Tbx5*$^{+}$/*Mef2cAHF*$^{+}$ lineage compared with controls (Fig. 6n–r), consistent with lineage mixing from boundary disruption and implicating a role for SLIT2 in maintaining boundary integrity. Conversely, homozygous *Ntn1* LOF mutants with the lineage reporter (*Tbx5*$^{CreERT2/+}$;*Mef2cAHF-DreERT2*;*ROSA26*$^{Ai66/+}$;*Ntn1*$^{-/-}$) showed leftward displacement of the *Tbx5*$^{+}$/*Mef2cAHF*$^{+}$ lineage compared with controls (Fig. 6s–v), implying that NTN1 signaling precisely positions the compartment boundary at the IVS. Taken together, this evidence suggested that SLIT2 and NTN1 signaling, as part of a Tbx5-dependent pathway, regulates the position and integrity of the compartment boundary labeled by the *Tbx5*$^{+}$/*Mef2cAHF*$^{+}$ lineage (Fig. 6w).

Discussion

We show that *Tbx5*$^{+}$/*Mef2cAHF*$^{+}$ progenitors prefigure a compartment boundary that becomes located at the junction between the left and right sides of the IVS, providing a cellular framework during development for heart patterning. Our study underscores a fundamental principle that early developmental events preconfigure the structure and function of the heart and are susceptible to genetic risks that cause CHDs. Furthermore, our results show developmental regulation of a compartment boundary by a disease-associated transcription factor and that aberrant tissue patterning from boundary disturbances may be an etiology of birth defects. This study reiterates the importance of compartment boundaries in tissue patterning, provides evidence for compartment boundary disruptions as an etiology of birth defects and adds to the few examples of compartment boundaries that exist in mammals.

We surmise that the rarity of compartment boundaries in mammals probably stems from a few reasons. The discovery of a compartment boundary was made by studying the fate of marked mosaic cells and their clonal segregation in the wing disk of the fly embryo[59]. Subsequent examples of compartment boundaries were identified by broad genetic screens in *Drosophila*[60]. In mammals, compartment boundaries were discovered by lineage analysis informed by another organism[33] or serendipitously[30], as we have done here. Compartment boundaries have been defined by several criteria. First, a compartment boundary segregates juxtaposed cell populations such as distinct cell lineages to restrict cell intermingling, and ablation of the boundary leads to cell mixing. Second, the expression domain of a selector gene corresponds with a compartment domain, loss of the selector gene eliminates the identity in this territory, and ectopic expression of the selector induces this identity. Third, a selector gene establishes a signaling center to maintain the compartments and boundary. Our results satisfy all of these criteria: ablation of the *Tbx5*$^{+}$/*Mef2cAHF*$^{+}$ lineage disrupts segregation of *Tbx5*$^{+}$ lineage cells in the LV from the *Tbx5*$^{-}$ lineage in the RV of the developing heart. Reduced *Tbx5* expression impairs the integrity of the boundary and its patterning, and in previous work, misexpression of TBX5 eliminates IVS formation[13]. Fourth, TBX5 patterns signaling molecules that are important for morphologies that impact the boundary. In this context, we postulate that *Tbx5* may function as a candidate selector gene. Further experiments will be needed to formally ascertain this.

In this context, we identify a *Tbx5*-dependent pathway that regulates *Slit2* and *Ntn1*. Normally, TBX5 represses their ectopic expression in the IVS and compact layer. Both SLIT2 and NTN1 are guidance or adhesive cues in several developmental contexts. Complete loss of *Slit2* causes perinatal lethality[61]. *Ntn1*$^{-/-}$ die around E11.5 (ref. 62) or E14.5 (ref. 56). Between E10.5 and E14.5, homozygous *Ntn1*$^{-/-}$ embryos showed absence of the ventral spinal commissure and a disorganized dorsal root entry zone[56].

Here we provide evidence that *Slit2* and *Ntn1* are direct targets of TBX5, and that *Tbx5* and *Slit2* or *Ntn1* genetically interact. Furthermore, we found that *Slit2* and *Ntn1* are essential for proper ventricular septation, as well as compartment boundary integrity and positioning, respectively. Like TBX5, proper ventricular septation may be sensitive to imbalanced dosage of SLIT2 or NTN1. Of note, mutations of *SLIT2* and the SLIT receptor *ROBO1* are associated with CHDs in mice and humans[49–52]. For NTN1, knockdown of *ntn1a* in zebrafish results in cardiovascular abnormalities[53], while *NTN1* had not yet been clearly implicated as a risk gene for mouse[62] or human CHDs[53]. Even so, *DSCAM*, which encodes a NETRIN co-receptor, is in the risk region for trisomy 21 (ref. 63), which often includes AV septal defects. Moreover, single nucleotide variants in *NEO1* and *UNC5B*, which encode NTN receptors, are associated with CHDs[64,65]. As mouse embryos from *Unc5b* loss, formerly known as *Unc5h2*, died of vascular abnormalities of the placenta by E12.5 (refs. 66,67), it remains unclear what role *Unc5b* might have in cardiac chamber formation and ventricular septation. As *Ntn1* expression is enriched in the LV and left side of the IVS in the *Tbx5*$^{+}$ compartment, we propose a working hypothesis that NTN1 may function as a TBX5-dependent signaling center for compartment boundary regulation.

The spatiotemporal position of the boundary is at the crux of cardiac septation and, when disrupted, spans sites for congenital cardiac anomalies. The sensitivity of the *Tbx5*$^{+}$/*Mef2cAHF*$^{+}$ lineage-labeled boundary to genetic perturbations, specifically *Tbx5* deficiency, is of relevance to the context of CHDs. Such deficiency selectively compromises the boundary's integrity and position, along with disturbances to cell orientation, leading to VSDs or AVSDs. These observations suggest that patterning during heart morphogenesis is exceptionally vulnerable to disruptions of gene dosage in early cardiac precursors. Early susceptibility could explain why CHDs arise at higher frequency than other birth defects. Thus, the *Tbx5*$^{+}$/*Mef2cAHF*$^{+}$ lineage provides a potential 'beacon' for understanding the cellular basis of septation defects. Whether additional genetic perturbations that cause VSDs or AVSDs disrupt the compartment boundary remains to be determined. Likewise, it will be interesting to evaluate whether the *Tbx5*$^{+}$/*Mef2cAHF*$^{+}$ lineage-labeled boundary corresponds with abnormal shifts in IVS position, such as those observed in the endothelial loss of *Hand2*, which shows a rightward-shifted IVS and a double-inlet left ventricle or two IVS primordia[68,69].

Several limitations of this study should be considered. Using inducible genetic tracing, there is an inherent variability from recombination of the fluorescent reporters within samples. For some comparisons, more samples of each genotype could have mitigated this limitation, but obtaining additional samples has been technically challenging, in large part owing to the requirement of five alleles to be present. Notwithstanding, we have tried to account for recombination efficiency, when possible, in imaging analyses. We have made great effort to mitigate this concern by not quantifying measurements that would be greatly skewed by recombination efficiency. For this reason, for example, we have refrained from commenting on whether a given lineage is quantitatively increased or decreased if fewer samples were available. Instead, we have focused our analyses on the location of the cells, as we feel that this is less affected by recombination efficiency. Using orthogonal approaches, we measure in an unbiased and statistically robust fashion using various metrics of quantitative morphometry from lightsheet or histology images. Our interpretations are based on statistical robustness from a large number of sampled regions per embryo, in the comparisons that are presented. The repeated measurements are akin to the (much larger) measurements in scRNA-seq.

Broadly, our study shows the delicate interplay of progenitor cell behavior, gene expression and compartment boundary formation that determines heart development and genetic susceptibility that increases the risk of CHDs. This evidence further underscores the importance of early developmental stages for the ontogeny of

some CHDs. Whether the extent of interaction between progenitor fields, migration of heart progenitors or formation of the boundary may contribute stochastically to phenotypic variation observed as a frequent feature of CHD genetics in mice or humans remains unclear. The implications of these discoveries probably extend beyond cardiac morphogenesis, as these findings offer insights for the roles of compartment boundaries during mammalian development and uncover a vulnerability for organ patterning from genetic disturbances.

Methods

Mouse lines

All mouse protocols (AN203375-00H and AN199784-00E) were approved by the Institutional Animal Care and Use Committee at University of California, San Francisco (UCSF). Mice were housed in a barrier animal facility with standard husbandry conditions (dark–light cycle, ambient temperature and humidity) at the Gladstone Institutes. Mice of *Tbx5*^{CreERT2IRES2xFLAG} (abbreviated here as *Tbx5*^{CreERT2}) and *Mef2cAHF-DreERT2* (ref. 25), *Tbx5*$^{del/+}$ and *Tbx5*$^{flox/+}$ (ref. 45), and *ROSA26*^{Ai66} and *ROSA26*^{Ai6} (ref. 35) were described previously. *Mef2cAHF-Cre* mice[46] were obtained from B. Black (UCSF). *Slit2*$^{+/-}$ mice (MMRC, strain 065588-UCD, donated by K. Lloyd, UC Davis) were generated by CRISPR–Cas9-targeted constitutive deletion of exon 8 and flanking splicing regions of *Slit2*. *Ntn1*$^{+/-}$ mice were derived from matings of *Ntn1* floxed mice (*Ntn1*$^{flox/+}$; Jackson Laboratory 028038)[56] to *beta-actin-Cre*[57], which were obtained from G. Martin (UCSF). All mouse strains were maintained in the C57BL6/J background (Jackson Laboratory 664), except for *Tbx5*$^{del/+}$, which was maintained in Black Swiss (Charles River, strain code 492), and *Slit2*$^{+/-}$, which was maintained in C57BL6/N (Jackson Laboratory, 005304). Both male and female embryos were collected from timed matings and used at random for experiments. Tamoxifen (Sigma-Aldrich; T5648) was suspended in sesame oil at 10 mg ml^{-1}. The injected dose was 100 µg g^{-1} body weight.

Cloning and generation of mouse lines

We generated an attenuated diptheria toxin (DTA176) transgenic knock-in mouse under the control of the dual-recombinase intersectional cassette. DTA176 encodes an attenuated form of toxic fragment A from diptheria toxin[36,37], which requires ~100–200 molecules for cell killing. This strategy was an effort to reduce potential problems of leaky DTA expression before recombinase-mediated activation. Briefly, *DTA176* (ref. 37) was cloned downstream of the ROX-STOP-ROX and LOX-STOP-LOX sites to create a Dre- and Cre-dependent expression construct, which was derived from the Dre- and Cre-dependent tdTomato expression cassette of the Ai66 (RCRL-tdT) targeting vector[35]. After the tdTomato cassette was removed using MluI sites and replaced by DTA176, the construct was cloned into the TARGATT targeting construct pBT346.3 (Applied Stem Cells) to target the transcriptionally inactive *Hip11* locus[70] using PacI and SmaI restriction enzyme sites. The final construct was verified using restriction digestion and Sanger sequencing. DNA was purified and injected along with mRNA for the Phi31o transposase according to the manufacturer's protocol to generate intersectional-DTA mutant (*Hip11*$^{Rox\text{-}STOP\text{-}Rox\text{-}Lox\text{-}STOP\text{-}Lox\text{-}DTA176}$) mice. To generate Ai66b mice (*ROSA26*^{Ai66b}), which is a Dre-dependent tdTomato reporter, the LOX-STOP-LOX sites were removed from the Ai66 (RCRL-tdT) targeting vector[35], and then the transgene cassette was inserted into endogenous genomic loci via homologous recombination, as previously described[71].

Whole-mount embryo and heart immunofluorescence labeling

Embryos were dissected from timed pregnant dams, including removal of the yolk sac for genotyping, as previously described[25]. Embryos staged up to E10.5 were fixed for 4 h in 4% PFA at room temperature, then incubated with gentle rocking in clearing solution (8% SDS in 0.2 M sodium borate buffer, pH 8.5) at 37 °C for 1–3 h until clear. E13.5 to E14.5 hearts were microdissected from freshly collected embryos in PBS with heparin (10 units ml^{-1}) (Sigma H3393) or incubated in 1× RBC lysis solution (Roche 11814389001) for 10 min at room temperature, fixed at room temperature in 4% PFA for 1 h and incubated with gentle rocking in clearing solution at 37 °C for 2–4 days until clear. Specimens were permeabilized and blocked for 2 h to overnight with gentle rocking at 37 °C in blocking buffer (PBS containing 5% normal donkey serum and 0.8–1.5% Triton X-100, dependent on the embryo or heart stage). Specimens were labeled with primary antibody (list below) in blocking buffer with gentle rocking at 37 °C, either overnight for embryos with stages up to E10.5 or for 5 days for E13.5 or E14.5 hearts. For long incubations, antibody solution was replaced halfway. Following three washes using blocking buffer, with the first two lasting 45 min each and the third third wash performed overnight for E13.5 and E14.5 hearts, the specimens were incubated with secondary antibody (raised in donkey; AF488, Dy405, Cy3 or AF647 conjugated; used at 1:750; Jackson ImmunoResearch) and DAPI in blocking buffer with gentle rocking at 37 °C, 2–3 h for embryos up to E10.5 or 5 days for E13.5 or E14.5 hearts. Following three washes in PBS with gentle rocking at 37 °C, samples were stored (up to overnight) in PBS with 0.2% sodium azide. The primary antibodies used were tdTomato (rabbit, Rockland 600-401-379, 1:1,000), MEF2c (sheep, R&D AF6786, 1:250) and TNNT2 (mouse, Thermo MS-295-P, 1:500). Strong ZsGreen fluorescence persisted after clearing and did not require immunolabeling.

Lightsheet image acquisition

Images were acquired by lightsheet microscopy, as described previously[72]. Briefly, specimens were warmed and transferred to 2% low-melting-point agarose (Fisher BP165-25) in PBS at 37 °C, then embedded in glass capillary tubes with paired pistons (Sigma Z328510 paired with BR701938, or Sigma Z328502 paired with BR701934) for embryos or tip-truncated 1-ml syringes (Becton Dickinson) for hearts. After the gel solidified, the capillaries or syringes were suspended, specimen down, from 14-ml polystyrene tubes sealed with Parafilm. Columns containing the specimen were partially extended into an ample volume of optical clearing solution (OCS, EasyIndex EI-Z1001, LifeCanvas) overnight. Following overnight incubation in OCS, specimen capillaries were retracted and brought to a LightSheet Z.1 microscope coupled with standard-issue laser lines and filter configurations, as well as dual pco.edge 4.2 cameras, with ZEN software (Carl Zeiss Imaging). Using immersion in OCS, specimens were imaged with a multi-view whole-volume approach, using one of two objective setups: EC Plan Neofluar 5X/0.16 with 5X/0.1 pair (hearts) or Clr Plan Neofluar 20X/1.0 paired with 10X/0.2 clearing pair (embryos). Z-stacks were collected at each view angle at the optimal slice thickness determined by Zeiss' Zen software, ranging from 1.42 µm to 4.95 µm.

Image dataset preprocessing

Imaging data were processed as previously described[72]. All of the data processing was performed on an 8-core x86-64 desktop PC with 64 GB RAM, running Kubuntu 20.04 LTS, principally using Fiji software[73]. Acquired lightsheet image stacks were subjected to single-view deconvolution using regularized generalized Tikhonov filtering (Parallel Spectral Deconvolution, https://imagej.net/plugins/parallel-spectral-deconvolution) following theoretical PSF calculation using the intersection of Gaussian *z*-plane illumination with Gibson–Lanni widefield epifluorescence detection patterns[74]. Deconvolved stacks were co-registered, and image volumes were generated for each desired orientation, for each specimen, using Content Based Fusion in BigStitcher[75]. TrackMate[76] and ImageJ 3-D viewer were used for segmentation and visualization of fused volumes.

Image volume quantification

Extensive whole-volume quantifications of imaged E14.5 hearts were performed using Fiji and associated plugins, with analysis conducted with R. For assessing the location of fluorescence signals, volumes

were downsampled, and two-dimensional regions of interest (ROIs) corresponding to anatomic structures were manually drawn on each Z-slice, using the DAPI channel in a single blinded fashion. Integrated intensity for each fluorescence channel was programatically measured for each ROI, and counts were normalized to the DAPI signal and pooled by anatomic region. For whole-heart quantifications, counts were further normalized to combined Ai6 plus Ai66 signal, then averaged across each anatomic region. For orientation assessments, a multichannel panel of 174 full-resolution four-chamber image excerpts, evenly distributed between apical–posterior, apical–anterior, posterior–basal and posterior–apical IVS, was split by channel (tdTomato or ZsGreen) and blindly sampled. Using automated batch processing, these samples were subjected to automated background filtering, including contrast enhancement, and measurements of orientation coherency (OrientationJ plugin, https://github.com/Biomedical-Imaging-Group/OrientationJ), and of dominant direction and 'directionality' score (Directionality plugin, https://github.com/fiji/Directionality). Directionality score distributions were rotated so that the dominant direction was set to 0°, with the average score (across the panel of images) plotted as a function of direction, with testing of the distribution by the Watson U2 test (R circular package) and analyzed by Watson's two-sample test. Individual scores surrounding 0° (±5°), 90° (±5°) and 65° (±20°) were pooled and compared with the Wilcoxon signed-rank test. As an alternative measure, orientation coherency scores across the panel of images were plotted by genotype and compared with the Wilcoxon signed-rank test.

Quantification of the right–left position of lineages

For each E10.5 heart analyzed, five representative coronal optical sections were selected, approximately 20–35 µm apart. For each optical section, the DAPI channel was used to draw five linear profiles spanning the ventricular chambers from right to left. Linear profiles were drawn such that the '0' position corresponded to the midline, identified by the IV groove. The fluorescence intensity of each channel (green, *Tbx5*$^+$ lineage; magenta, *Mef2cAHF*+ lineage) was measured along each linear profile, and intensity values were normalized to the maximum value along each profile. Profiles for each channel were grouped by experimental condition (WT or DTA), and then the average ± s.e.m. normalized fluorescence intensity profiles were calculated and plotted. Welch's two-sample *t*-test was used at each position along the right–left axis to determine regions of significant difference in fluorescence intensity of each channel between experimental groups, indicating a change in the distribution of cells of that lineage.

The same images and *Z*-slices were also analyzed for the percentage distribution of the green, *Tbx5*$^+$, and magenta, *Mef2cAHF*$^+$, lineages across the ventricles. ROIs were assigned using the DAPI channel to subset the left and right ventricles using the IV groove as a landmark. The percentage area was calculated using the area of the green or magenta signal and the total ventricular area. These values were normalized per *Z*-slice to the total area of signal in both ventricles. Significance was measured using *t*-tests.

For each E13.5–E14.5 heart analyzed, maximum *Z*-projections were generated from optical sections spanning every 50 µm (E13.5–E14.0) or 100 µm (E14.5) from the anterior to posterior of the heart. For each maximum *Z*-projection, the DAPI and magenta (*Tbx5*$^+$/*Mef2cAHF*$^+$ intersectional lineage) channels were split and background subtraction was performed on the magenta channel using a 50-pixel rolling ball radius. The DAPI channel was used to draw three linear profiles (basal, middle, apical) spanning the ventricular chambers from right to left. Linear profiles were drawn such that the '0' position corresponded to the middle of the IVS. Fluorescence intensity of the magenta channel was measured along each linear profile, and intensity values were normalized to the maximum value along each profile. Profiles were grouped by experimental condition (*Tbx5*$^{CreERT2/+}$ or *Tbx5*$^{CreERT2/flox}$) or, for example, WT, *Ntn1*$^{+/-}$ or *Ntn1*$^{-/-}$, and then the average ± s.e.m. normalized fluorescence intensity profiles were calculated and plotted. Two-sample *F*-test and Welch's *t*-test were used to analyze the distribution of *Tbx5*$^+$/*Mef2cAHF*$^+$ intersectional lineage cells.

Cell collecting for scRNA-seq

Samples for scRNA-seq were collected from three independent litters at E13.5. The heart was microdissected to obtain the IVS, and left ventricular or right ventricular regions. The control samples were *Tbx5*$^{CreERT2/+}$;*Mef2cAHF-DreERT2;ROSA26*$^{Ai66/Ai6}$ ($n = 3$) and *Tbx5*$^{CreERT2/+}$;*Mef2cAHF-DreERT2;ROSA26*$^{Ai66/+}$ ($n = 1$) for the LV, RV and IVS each. *Tbx5* mutant samples were *Tbx5*$^{CreERT2/flox}$;*Mef2cAHF-DreERT2;ROSA26*$^{Ai66/Ai6}$ for the RV and LV ($n = 3$ each) and IVS ($n = 2$). One *Tbx5* mutant sample of the IVS + AVco regions was not included because it was lost from a microfluidic chip clog during sample processing.

Each microdissected tissue was singularized with TrypLE Express (Life Technologies, catalog number 12604-013) at 37 °C and quenched with 1% FBS in PBS. The single-cell suspension was then filtered through a cell strainer cap (Corning, catalog number 352235) and centrifuged at 300 *g* for 5 min. The pellet was resuspended in 1% FBS in PBS, and the cells were counted using an automated cell counter. A 30-µl aliquot of the cell suspension was used to generate single-cell droplet libraries with the Chromium Next GEM Single Cell 5′ Library and Gel Bead Kit v1.1, according to the manufacturer's instructions (10X Genomics). After KAPA qPCR quantification, a shallow sequencing run was performed on a NextSeq 500 (Illumina) before deep sequencing on a NovaSeq S4 (Illumina). For control IVS + AVco regions, at E13.5, three samples were *Tbx5*$^{CreERT2/+}$;*Mef2cAHF-DreERT2;ROSA26*$^{Ai66/Ai6}$.

Data processing using Cell Ranger

All datasets were processed using Cell Ranger 2.0.2. FASTQ files were generated using the mkfastq function. Reads were aligned to a custom mm9 reference (version 1.2.0) containing *tdTomato* and *ZsGreen* reporter genes. Cell Ranger aggr was used to aggregate individual libraries after read depth normalization.

Seurat analysis

Outputs from the Cell Ranger pipeline were analyzed using Seurat v3 (refs. 77–79). Datasets from the IVS, LV and RV were analyzed separately. Cells with 10,000–50,000 UMIs and 1,500–7,250 genes were retained. Data were normalized using the NormalizeData function and scaled using ScaleData, while also regressing unwanted sources of variation, such as differences in the number of UMIs, number of genes and percentage of mitochondrial reads and differences between G2M and S phase scores. Principal component analysis was performed using the most highly variable genes. Cells were then clustered based on the top 30 principal components and visualized on a uniform manifold approximation and projection (UMAP)[80]. A clustering resolution that separated cells by major cell types was chosen. Next, *Tnnt2*$^+$ clusters from the IVS dataset were extracted and re-clustered, similar to the parent dataset above. A clustering resolution was chosen based on separation of genotypes. Differential gene expression tests between clusters or between *ZsGreen*$^+$ and *ZsGreen*$^-$ or *tdTomato*$^+$ and *tdTomato*$^-$ cells were performed using the FindMarkers function with default parameters. Selected differentially expressed genes with an adjusted *P* value less than 0.05 from the Wilcoxon rank sum test were shown using the Dotplot or FeaturePlot functions.

Fluorescence in situ hybridization

E11.5 or E14.5 hearts were fixed with 4% paraformaldehyde or 10% formalin overnight at 4 °C, embedded in paraffin and then sectioned for a transverse or four-chambered view on slides. In situ hybridization was performed on sections using the RNAscope Multiplex Fluorescent v2 Assay kit (Advanced Cell Diagnostics, catalog number 323100). Briefly, sections were deparaffinized in xylene and 100% ethanol, treated with hydrogen peroxide for 10 min and boiled in target retrieval buffer for

10 min. A hydrophobic barrier was drawn around each section using an Immedge pen (Vector Laboratories, catalog number H-4000), and slides were allowed to dry overnight. The following day, sections were treated with Protease Plus for 30 min, followed by hybridization with probes for 2 h at 40 °C. Probes (Advanced Cell Diagnostics) used were *Mm-Tnnt2-C4* (catalog number 418681-C4), *Mm-Ntn1* (catalog number 407621), *Mm-Slit2* (catalog number 449691), *Mm-Nppa-C3* (catalog number 418691-C3), *Mm-Bmp2-C2* (catalog number 406661-C2), *Mm-Robo1* (catalog number 475951), *Mm-Unc5b* (catalog number 482481) and *Mm-Irx2* (catalog number 519901). Amplification steps were carried out according to the manufacturer's instructions. Opal dyes 520, 570, 620 and 690 (Akoya Biosciences, catalog numbers FP1487001KT, FP1487001KT, FP1487001KT and FP1487001KT) were used at 1:750 dilution. After DAPI staining, one to two drops of ProLong Gold Antifade Mountant (Thermo Fisher Scientific, catalog number P36930) were placed on the slides, and the slides were mounted with coverslips. The slides were stored overnight at 4 °C and imaged at ×10 magnification on the Olympus FV3000RS. Multi-area time lapse images were captured and then stitched together using the Olympus FV3000RS software. The stitched images were analyzed using the ImageJ OlympusViewer plugin.

Immunohistochemistry

Cryopreserved slides were thawed from −80 °C at room temperature (RT) and washed in 0.1% Triton X-100 in PBS (PBST) three times, 5 min per wash. Antigen retrieval was performed by boiling slides in 10 mM sodium citrate buffer (pH 6.0) for 10 min and then washing in H_2O three times, 5 min per wash. Blocking was performed using 5% donkey serum in 0.1% PBST at RT for 1–2 h. Anti-Netrin-1 antibody 1:500 (R&D Systems AF1109) in 1% BSA + 0.1% PBST was incubated at 4 °C overnight. After washing three times for 5 min per wash in 0.1% PBST, the slides were incubated in Alexa Fluor 594 (1:300) in 1% BSA + 0.1% PBST at RT for 1 h. The slides were then washed three times, 5 min per wash, in 0.1% PBST and incubated in 1:1,000 DAPI in 0.1% PBST at RT for 5–10 min. Finally, the slides were washed three times, 5 min per wash, in 0.1% PBST, glass coverslips were mounted using Prolong Gold antifade mounting medium, and the slides were stored at 4 °C.

Quantification of IVS cell size and shape by WGA staining

Blind measurements of IVS cell size and shape were made on 5-µm paraffin-embedded *Tbx5*$^{CreERT2/+}$ or *Tbx5*$^{CreERT2/flox}$ hearts at E14.5, sectioned in four-chamber view approximately midway in the anterior–posterior axis. After sectioning, slides were stained for cardiac troponin T (cTNT, 1:500 cTNT, Thermo, MS-295-P) using Alexa 488 donkey anti-mouse secondary antibody (Jackson Immunoresearch), in addition to Alexa 594-conjugated WGA (dilution 5 µM, Thermo, W11262) and DAPI. After widefield imaging on a confocal fluorescence microscope at ×40, ROIs from the apical, basal and mid regions of the IVS were extracted in both DAPI and WGA channels, guided by cTNT staining as an anatomic reference. ROIs from the DAPI channel were subjected to automatic segmentation and counting to assess cell number and density. ROIs from the WGA channel were scrambled for blinding *Tbx5* genotype, and 24–56 easily identified cell bodies per ROI (depending on ROI size) were manually assessed in Fiji for length, width and axis orientation. Taking cell bodies as roughly elliptical, their diameter, area and eccentricities were estimated, and *Tbx5* genotype identities were unscrambled for plotting. Scripts for the filename scrambling–unscrambling, as well as automated quantification and count tallying, as described above, are available at Github (https://github.com/mhdominguez/Kathiriya-NCVR-2026-analysis).

Machine learning-based 3-D reconstruction from histology and quantitative micrometry

Tissues were formalin fixed, paraffin embedded and serially sectioned at a standard thickness of 5 µm to exhaustively collect the heart tissue of each fetal mouse. Serial sections were stained with hematoxylin and eosin and digitized at ×20 magnification using a Leica Versa 200 Automated Slide Scanner. CODA, a technique to 3-D reconstruct serial tissue images, was used to map the microanatomy of the hearts[58,81]. The various steps of CODA can be broken down into image registration, nuclear detection and tissue labeling. Nonlinear image registration was used to align the serial images. Cellular coordinates were generated through color deconvolution and detection of two-dimensional intensity peaks in the hematoxylin channel of the images. A deep learning semantic segmentation algorithm was trained to label the anatomical structures of the mice at 1-µm resolution. To train the model, manual annotations of six structures were generated in 55 histological images corresponding to the different large structures present in the tissue: bones, spinal cord, lung, liver, stroma, heart and non-tissue pixels in the images. A second deep learning model was trained to subclassify the ROIs within the heart: compact myocardium, trabeculae, IVS, AVco region and atria. Fifty images from the manual annotation datasets were used for model training, with five images held out for independent testing of model accuracy. The models were deemed acceptable when they reached a minimum per-class precision and recall of >85%. Independent images were segmented using the trained model and aligned to generate digital 3-D datasets.

The reconstructed volumes enabled microanatomical quantification of anatomical properties. IVS fill, or the solidity of the muscle layer in the IVS, was calculated by dividing the number of dark (<200 in RBG color space) pixels within the IVS, normalized by all pixels (including empty space) within the IVS. Percentage trabeculation within the IVS was calculated by isolating the tissue classified as trabeculae that was spatially attached to the IVS, then normalizing this number by the combined volume of trabeculae attached to IVS and the volume of the IVS itself. The compact myocardium thickness was calculated by measuring the thickness of the compact layer at the bottom 20% of the ventricles. To measure the thickness on the left and right ventricles, the two sides of the heart were manually segmented in 3-D space. VSDs were identified by calculating regions where the empty space of the LV contacted the empty space of the RV. These defects were evaluated and manually sorted into membranous or muscular subtypes. The areas of each defect were then manually calculated through annotation on serial histological images representing the shortest path to close the defect. These lines were summed across all images containing the defect multiplied by the thickness of the histological slides to determine the area of the hole.

Statistics and reproducibility

For statistical analysis of genetic interactions, the number of animals with a given defect (muscular VSD or membranous VSD) was modeled in a generalized linear model assuming a binomial probability distribution for the observed counts. This model included main effects (in terms of log odds ratios) capturing the number of mutant alleles for *Tbx5* (0 or 1, representing the WT or the Het genotype, respectively) and the number of mutant alleles for *Slit2* or *Ntn1* (0, 1 or 2, representing the WT, Het or Hom genotype, respectively) and an interaction between these effects. Given the relatively small number of animals in this experiment, bias-reduced estimates were made using the brglm2 package (Kosmidis.2020)[82] in R.

Representative images are shown, based on experiments that were repeated independently with similar results, as follows: Fig. 1a–f, 2 samples; Fig. 1g,j, 5 samples; Fig. 2a–i, 4 samples; Fig. 2j–n, 6 samples; Fig. 2o–q, 8 samples; Fig. 2r,t, 15 samples; Fig. 3a,b, 2 controls, 2 *DTA* mutants; Fig. 3c–j, 2 controls, 4 *DTA* mutants; Fig. 3l–n(i) and Extended Data Fig. 2, 3 controls, 2 *DTA* mutants; Extended Data Fig. 4a–d, 5 controls and 4 *Tbx5* mutants, for which some samples are shown in Extended Data Fig. 4a–i; Fig. 4i–m, 4 controls; Fig. 4n–r, 3 *Tbx5* mutants; Fig. 4u,v(i), 2 controls, 2 *Tbx5* mutants; 5i–n; 2 controls and 2 *Tbx5* mutants, for which the second replicates are shown in

Extended Data Fig. 6i–n(ii); Fig. 6f–h, 14 controls, 8 *Slit2*$^{+/-}$, 4 *Slit2*$^{-/-}$; Fig. 6j–l, 14 controls, 9 *Ntn1*$^{+/-}$, 7 *Ntn1*$^{-/-}$, with some samples shown in Extended Data Fig. 10a–d; Extended Data Fig. 1, 2 samples per condition; Extended Data Fig. 4a–l, 5 controls, 4 *Tbx5* mutants, with some samples shown in Fig. 4; Extended Data Fig. 3, 3 controls, 7 *Tbx5* mutants; Extended Data Fig. 6a–h(i), 2 controls and 2 *Tbx5* mutants; Extended Data Fig. 6o, 2 controls; Extended Data Fig. 7a–h, 2 controls and 2 *Tbx5* mutants; Extended Data Fig. 9a–d, 14 controls, 8 *Tbx5*$^{+/-}$, 8 *Slit2*$^{+/-}$; 8 *Tbx5*$^{+/-}$; *Slit2*$^{+/-}$; and Extended Data Fig. 9f–i, 14 controls, 7 *Tbx5*$^{+/-}$; 9 *Ntn1*$^{+/-}$, 7 *Ntn1*$^{-/-}$. Supplementary Fig. 1, 5 samples; Supplementary Fig. 2, 5 controls, 4 *Tbx5* mutants; and Supplementary Fig. 3, 2 controls, 2 *Tbx5* mutants.

Reporting summary

Further information on research design is available in the Nature Portfolio Reporting Summary linked to this article.

Data availability

The scRNA-seq data generated in this paper are available in the NCBI GEO database (GSE260601). ChIP-seq data from ref. 55 are available in the GEO database (GSE124008). Source data are provided with this paper.

Code availability

Code related to 'image volume quantification'[72] is available via GitHub at https://github.com/mhdominguez/LSFMProcessing. Source data and scripts used to analyze other morphometrics from lightsheet microscopy, such as right–left positioning, orientation and directionality of cells, are available via GitHub at https://github.com/mhdominguez/Kathiriya-NCVR-2026-analysis.

References

1. Kirby, R. S. The prevalence of selected major birth defects in the United States. *Semin. Perinatol.* **41**, 338–344 (2017).
2. Linde, D. vander et al. Birth prevalence of congenital heart disease worldwide: a systematic review and meta-analysis. *J. Am. Coll. Cardiol.* **58**, 2241–2247 (2011).
3. Liu, Y. et al. Global birth prevalence of congenital heart defects 1970–2017: updated systematic review and meta-analysis of 260 studies. *Int. J. Epidemiol.* **48**, 455–463 (2019).
4. Cohen, M. S. & Spray, T. L. Surgical management of unbalanced atrioventricular canal defect. *Semin. Thorac. Cardiovasc. Surg. Pediatr. Card. Surg. Annu.* **8**, 135–144 (2005).
5. Cruz, M. V. dela, Castillo, M. M., Villavicencio, L., Valencia, A. & Moreno-Rodriguez, R. A. Primitive interventricular septum, its primordium, and its contribution in the definitive interventricular septum: in vivo labelling study in the chick embryo heart. *Anat. Rec.* **247**, 512–520 (1997).
6. Harh, J. Y. & Paul, M. H. Experimental cardiac morphogenesis: I. Development of the ventricular septum in the chick. *Development* **33**, 13–28 (1975).
7. Ben-Shachar, G., Arcilla, R. A., Lucas, R. V. & Manasek, F. J. Ventricular trabeculations in the chick embryo heart and their contribution to ventricular and muscular septal development. *Circ. Res.* **57**, 759–766 (1985).
8. Contreras-Ramos, A., Sánchez-Gómez, C., García-Romero, H. L. & Cimarosti, L. O. Normal development of the muscular region of the interventricular septum—I. The significance of the ventricular trabeculations. *Anat. Histol. Embryol.* **37**, 344–351 (2008).
9. Wessels, A. et al. Spatial distribution of "tissue-specific" antigens in the developing human heart and skeletal muscle. I. An immunohistochemical analysis of creatine kinase isoenzyme expression patterns. *Anat. Rec.* **228**, 163–176 (1990).
10. Wessels, A. et al. The development of the atrioventricular junction in the human heart. *Circ. Res.* **78**, 110–117 (1996).
11. Lamers, W. H. et al. New findings concerning ventricular septation in the human heart. Implications for maldevelopment. *Circulation* **86**, 1194–1205 (2018).
12. Meilhac, S. M., Esner, M., Kerszberg, M., Moss, J. E. & Buckingham, M. E. Oriented clonal cell growth in the developing mouse myocardium underlies cardiac morphogenesis. *J. Cell Biol.* **164**, 97–109 (2004).
13. Koshiba-Takeuchi, K. et al. Reptilian heart development and the molecular basis of cardiac chamber evolution. *Nature* **461**, 95–98 (2009).
14. Christoffels, V. M., Keijser, A. G. M., Houweling, A. C., Clout, D. E. W. & Moorman, A. F. M. Patterning the embryonic heart: identification of five mouse iroquois homeobox genes in the developing heart. *Dev. Biol.* **224**, 263–274 (2000).
15. Stadtfeld, M., Ye, M. & Graf, T. Identification of interventricular septum precursor cells in the mouse embryo. *Dev. Biol.* **302**, 195–207 (2007).
16. Cruz, M. V. dela, Sánchez-Gómez, C. & Palomino, M. A. The primitive cardiac regions in the straight tube heart (stage 9) and their anatomical expression in the mature heart: an experimental study in the chick embryo. *J. Anat.* **165**, 121–131 (1989).
17. Moorman, A., Webb, S., Brown, N. A., Lamers, W. & Anderson, R. H. Development of the heart: (1) formation of the cardiac chambers and arterial trunks. *Heart* **89**, 806–814 (2003).
18. Laura, V. G. et al. Incorporation of the first and second heart fields and prospective fate of the straight heart tube via in vivo labeling of chicken embryos. *PLoS ONE* **15**, e0234069-17 (2020).
19. Franco, D., Kelly, R., Lamers, W. H., Buckingham, M. & Moorman, A. F. M. Regionalized transcriptional domains of myosin light chain 3f transgenes in the embryonic mouse heart: morphogenetic implications. *Dev. Biol.* **188**, 17–33 (1997).
20. Cai, C.-L. et al. Isl1 identifies a cardiac progenitor population that proliferates prior to differentiation and contributes a majority of cells to the heart. *Dev. Cell* **5**, 877–889 (2003).
21. Meilhac, S. M., Esner, M., Kelly, R. G., Nicolas, J.-F. & Buckingham, M. E. The clonal origin of myocardial cells in different regions of the embryonic mouse heart. *Dev. Cell* **6**, 685–698 (2004).
22. Liang, X. et al. HCN4 dynamically marks the first heart field and conduction system precursors. *Circ. Res.* **113**, 399–407 (2013).
23. Später, D. et al. A HCN4+ cardiomyogenic progenitor derived from the first heart field and human pluripotent stem cells. *Nat. Cell Biol.* **15**, 1098–1106 (2013).
24. Lescroart, F. et al. Early lineage restriction in temporally distinct populations of Mesp1 progenitors during mammalian heart development. *Nat. Cell Biol.* **16**, 829–840 (2014).
25. Devine, W. P., Wythe, J. D., George, M., Koshiba-Takeuchi, K. & Bruneau, B. G. Early patterning and specification of cardiac progenitors in gastrulating mesoderm. *Elife* **3**, 508 (2014).
26. Lescroart, F. et al. Defining the earliest step of cardiovascular lineage segregation by single-cell RNA-seq. *Science* **359**, 1177–1181 (2018).
27. Kiecker, C. & Lumsden, A. Compartments and their boundaries in vertebrate brain development. *Nat. Rev. Neurosci.* **6**, 553–564 (2005).
28. Dahmann, C., Basler, K., Dahmann, C. & Basler, K. Compartment boundaries: at the edge of development. *Trends Genet.* **15**, 320–326 (1999).
29. Wang, J. & Dahmann, C. Establishing compartment boundaries in *Drosophila* wing imaginal discs: an interplay between selector genes, signaling pathways and cell mechanics. *Semin. Cell Dev. Biol.* **107**, 161–169 (2020).
30. Kimmel, R. A. et al. Two lineage boundaries coordinate vertebrate apical ectodermal ridge formation. *Genes Dev.* **14**, 1377–1389 (2000).

31. Arques, C. G., Doohan, R., Sharpe, J. & Torres, M. Cell tracing reveals a dorsoventral lineage restriction plane in the mouse limb bud mesenchyme. *Development* **134**, 3713–3722 (2007).
32. Qiu, Q., Chen, H. & Johnson, R. L. Lmx1b-expressing cells in the mouse limb bud define a dorsal mesenchymal lineage compartment. *Genesis* **47**, 224–233 (2009).
33. Zervas, M., Millet, S., Ahn, S. & Joyner, A. L. Cell behaviors and genetic lineages of the mesencephalon and rhombomere 1. *Neuron* **43**, 345–357 (2004).
34. Franco, D. et al. Left and right ventricular contributions to the formation of the interventricular septum in the mouse heart. *Dev. Biol.* **294**, 366–375 (2006).
35. Madisen, L. et al. Transgenic mice for intersectional targeting of neural sensors and effectors with high specificity and performance. *Neuron* **85**, 942–958 (2015).
36. Maxwell, F., Maxwell, I. H. & Glode, L. M. Cloning, sequence determination, and expression in transfected cells of the coding sequence for the tox 176 attenuated diphtheria toxin A chain. *Mol. Cell. Biol.* **7**, 1576–1579 (2007).
37. Wu, S., Wu, Y. & Capecchi, M. R. Motoneurons and oligodendrocytes are sequentially generated from neural stem cells but do not appear to share common lineage-restricted progenitors in vivo. *Development* **133**, 581–590 (2006).
38. Erhardt, V. et al. Systematic optimization and prediction of cre recombinase for precise genome editing in mice. *Genome Biol.* **26**, 85 (2025).
39. Bao, J., Ma, H., Schuster, A., Lin, Y. & Yan, W. Incomplete Cre-mediated excision leads to phenotypic differences between *Stra8-iCre; Mov10l1*$^{lox/lox}$ and *Stra8-iCre; Mov10l1*$^{lox/\Delta}$ *mice*. *Genesis* **51**, 481–490 (2013).
40. Haldar, M., Karan, G., Tvrdik, P. & Capecchi, M. R. Two cell lineages, myf5 and myf5-independent, participate in mouse skeletal myogenesis. *Dev. Cell* **14**, 437–445 (2008).
41. Vincentz, J. W., Toolan, K. P., Zhang, W. & Firulli, A. B. Hand factor ablation causes defective left ventricular chamber development and compromised adult cardiac function. *PLoS Genet.* **13**, e1006922 (2017).
42. Basson, C. T. et al. Mutations in human TBX5 [corrected] cause limb and cardiac malformation in Holt–Oram syndrome. *Nat. Genet.* **15**, 30–35 (1997).
43. Li, Q. Y. et al. Holt–Oram syndrome is caused by mutations in TBX5, a member of the Brachyury (T) gene family. *Nat. Genet.* **15**, 21–29 (1997).
44. Kathiriya, I. S. et al. Modeling human TBX5 haploinsufficiency predicts regulatory networks for congenital heart disease. *Dev. Cell* **56**, 292–309.e9 (2021).
45. Bruneau, B. G. et al. A murine model of Holt–Oram syndrome defines roles of the T-box transcription factor Tbx5 in cardiogenesis and disease. *Cell* **106**, 709–721 (2001).
46. Verzi, M. P., McCulley, D. J., Val, S. D., Dodou, E. & Black, B. L. The right ventricle, outflow tract, and ventricular septum comprise a restricted expression domain within the secondary/anterior heart field. *Dev. Biol.* **287**, 134–145 (2005).
47. Mori, A. D. & Bruneau, B. G. TBX5 mutations and congenital heart disease: Holt–Oram syndrome revealed. *Curr. Opin. Cardiol.* **19**, 211–215 (2004).
48. Larrieu-Lahargue, F., Thomas, K. R. & Li, D. Y. Netrin ligands and receptors: lessons from neurons to the endothelium. *Trends Cardiovasc. Med.* **22**, 44–47 (2012).
49. Mommersteeg, M. T. M., Yeh, M. L., Parnavelas, J. G. & Andrews, W. D. Disrupted Slit–Robo signalling results in membranous ventricular septum defects and bicuspid aortic valves. *Cardiovasc. Res.* **106**, 55–66 (2015).
50. Agustin, J. T. S. et al. Genetic link between renal birth defects and congenital heart disease. *Nat. Commun.* **7**, 11103–11111 (2016).
51. Kruszka, P. et al. Loss of function in ROBO1 is associated with tetralogy of Fallot and septal defects. *J. Med. Genet.* **54**, 825 (2017).
52. Fotiou, E. et al. Integration of large-scale genomic data sources with evolutionary history reveals novel genetic loci for congenital heart disease. *Circ. Genom. Precis. Med.* **12**, 442–451 (2019).
53. Opitz, R. et al. Functional zebrafish studies based on human genotyping point to netrin-1 as a link between aberrant cardiovascular development and thyroid dysgenesis. *Endocrinology* **156**, 377–388 (2015).
54. Li, Y. et al. Global genetic analysis in mice unveils central role for cilia in congenital heart disease. *Nature* **521**, 520–524 (2015).
55. Akerberg, B. N. et al. A reference map of murine cardiac transcription factor chromatin occupancy identifies dynamic and conserved enhancers. *Nat. Commun.* **10**, 4907 (2019).
56. Bin, J. M. et al. Complete loss of netrin-1 results in embryonic lethality and severe axon guidance defects without increased neural cell death. *Cell Rep.* **12**, 1099–1106 (2015).
57. Lewandoski, M., Meyers, E. N. & Martin, G. R. Analysis of Fgf8 gene function in vertebrate development. *Cold Spring Harb. Symp. Quant. Biol.* **62**, 159–168 (1997).
58. Kiemen, A. L. et al. CODA: quantitative 3D reconstruction of large tissues at cellular resolution. *Nat. Methods* https://doi.org/10.1038/s41592-022-01650-9 (2022).
59. Vincent, J. P. Compartment boundaries: where, why and how?. *Int. J. Dev. Biol.* **42**, 311–315 (1998).
60. Lawrence, P. A. & Struhl, G. Morphogens, compartments, and pattern: lessons from drosophila?. *Cell* **85**, 951–961 (1996).
61. Plump, A. S. et al. Slit1 and Slit2 cooperate to prevent premature midline crossing of retinal axons in the mouse visual system. *Neuron* **33**, 219–232 (2002).
62. Matos-Nieves, A. et al. Expression of Netrin-1 in the developing mouse heart. *Gene Expr. Patterns* https://doi.org/10.1016/j.gep.2025.119398 (2025).
63. Barlow, G. M. et al. Down syndrome congenital heart disease: a narrowed region and a candidate gene. *Genet. Med.* **3**, 91–101 (2001).
64. Jin, S. C. et al. Contribution of rare inherited and de novo variants in 2,871 congenital heart disease probands. *Nat. Genet.* **49**, 1593–1601 (2017).
65. Dong, W. et al. Recessive genetic contribution to congenital heart disease in 5,424 probands. *Proc. Natl Acad. Sci. USA* **122**, e2419992122 (2025).
66. Lu, X. et al. The netrin receptor UNC5B mediates guidance events controlling morphogenesis of the vascular system. *Nature* **432**, 179–186 (2004).
67. Navankasattusas, S. et al. The netrin receptor UNC5B promotes angiogenesis in specific vascular beds. *Development* **135**, 659–667 (2008).
68. VanDusen, N. J. et al. Hand2 is an essential regulator for two notch-dependent functions within the embryonic endocardium. *Cell Rep.* **9**, 2071–2083 (2014).
69. George, R. M. et al. Single cell evaluation of endocardial HAND2 gene regulatory networks reveals critical HAND2-dependent pathways impacting cardiac morphogenesis. *Development* https://doi.org/10.1242/dev.201341 (2023).
70. Tasic, B. et al. Site-specific integrase-mediated transgenesis in mice via pronuclear injection. *Proc. National Acad. Sci. USA* **108**, 7902–7907 (2011).
71. Madisen, L. et al. A robust and high-throughput Cre reporting and characterization system for the whole mouse brain. *Nat. Neurosci.* **13**, 133–140 (2010).
72. Dominguez, M. H., Krup, A. L., Muncie, J. M. & Bruneau, B. G. Graded mesoderm assembly governs cell fate and morphogenesis of the early mammalian heart. *Cell* **186**, 479–496.e23 (2023).

73. Schindelin, J. et al. Fiji: an open-source platform for biological-image analysis. *Nat. Methods* **9**, 676–682 (2012).
74. Kirshner, H., Aguet, F., Sage, D. & Unser, M. 3-D PSF fitting for fluorescence microscopy: implementation and localization application. *J. Microsc.* **249**, 13–25 (2013).
75. Hörl, D. et al. BigStitcher: reconstructing high-resolution image datasets of cleared and expanded samples. *Nat. Methods* **16**, 870–874 (2019).
76. Tinevez, J.-Y. et al. TrackMate: an open and extensible platform for single-particle tracking. *Methods* **115**, 80–90 (2017).
77. Satija, R., Farrell, J. A., Gennert, D., Schier, A. F. & Regev, A. Spatial reconstruction of single-cell gene expression data. *Nat. Biotechnol.* **33**, 495–502 (2015).
78. Butler, A., Hoffman, P., Smibert, P., Papalexi, E. & Satija, R. Integrating single-cell transcriptomic data across different conditions, technologies, and species. *Nat. Biotechnol.* **36**, 411–420 (2018).
79. Stuart, T. et al. Comprehensive integration of single-cell data. *Cell* **177**, 1888–1902.e21 (2019).
80. Becht, E. et al. Dimensionality reduction for visualizing single-cell data using UMAP. *Nat. Biotechnol*. https://doi.org/10.1038/nbt.4314 (2018).
81. Forjaz, A. et al. Three-dimensional assessments are necessary to determine the true, spatially resolved composition of tissues. *Cell Rep. Methods* **5**, 101075 (2025).
82. Kosmidis, I. & Firth, D. Jeffreys-prior penalty, finiteness and shrinkage in binomial-response generalized linear models. *Biometrika* **108**, asaa052 (2020).

Acknowledgements

We dedicate this paper in memory of Tatyana Sukonnik (Gladstone Institutes). We thank B. Black (UCSF) for the *Mef2cAHF-Cre* mouse line and members of the Bruneau laboratory for troubleshooting help, discussions and comments. We also thank the Gladstone Bioinformatics, Genomics, and Histology and Microscopy Cores, the UCSF Laboratory for Cell Analysis and the UCSF Center for Advanced Technology. This study was supported by grants from the National Institutes of Health (NHLBI Bench to Bassinet Program UM1HL098179 to B.G.B.; R01HL114948 to B.G.B., R01HL155906 to B.G.B. and I.S.K., 1R56HL166894-01A1 to I.S.K., K99HL177318 to J.M.M.-V., U54CA268083 and UG3CA275681 to A.L.K.), also by a postdoctoral fellowship from the American Heart Association, together with The Children's Heart Foundation (24POST1191660) to J.M.M.-V., Additional Ventures Innovation Fund to B.G.B., Society for Pediatric Anesthesia (Young Investigator Award to I.S.K.), Hellman Family Fund (I.S.K.), UCSF REAC Grant (I.S.K.), Saving tiny Hearts Society to I.S.K., UCSF Pediatric Heart Center Catalyst Award to I.S.K. and UCSF Department of Anesthesia and Perioperative Care Research Support to I.S.K. This study was also supported by an NIH/NCRR grant (C06 RR018928) to the J. David Gladstone Institutes, and the Younger Family Fund (B.G.B.).

Author contributions

This study was originally conceived by W.P.D. and B.G.B. and refined and developed by I.S.K. and B.G.B. W.P.D. made initial observations using genetic lineage tools that he gathered or generated. I.S.K., M.H.D., W.P.D. and K.M.H. performed embryo dissections. K.M.H., B.I.G., P.G., M.N.M., T.S., D.M.-P., S.W. and E.F.B. managed animal husbandry and genotyping. I.S.K., M.H.D., W.P.D. and K.M.H. performed whole-mount or section immunostaining experiments and imaging. M.H.D., J.M.M.-V. and D.Q performed lightsheet imaging and processing, and M.H.D. and J.M.M.-V. implemented analyses with hypothesis-based input from I.S.K. I.S.K. designed the strategy to use a 5′ sequencing kit and developed synthetic genome with the Gladstone Bioinformatics core, microdissected heart regions for scRNA-seq and processed samples with K.S.R. and P.G. for sequencing library preparations. K.S.R. generated scRNA-seq libraries and performed scRNA-seq analyses with hypothesis-based input from I.S.K. K.S.R., K.M.H., P.G. and M.N.M. performed section in situ hybridization and imaging. K.S.R. generated ChIP-seq browser tracks with input from S.K.H. I.S.K. assessed cardiac defects by histology and provided anatomical knowledge to A.L.K. to apply a deep learning tool for cardiac morphometry. A.F. trained deep learning models and was supervised by A.L.K. and advised by P.-H.W. and D.W. B.G.B. supervised and advised the study. I.S.K. and K.S.R. prepared figures. I.S.K. wrote the original draft with contributions from the co-authors. I.S.K. and B.G.B. edited the paper with input from the co-authors.

Competing interests

B.G.B. is a co-founder and shareholder of Tenaya Therapeutics. B.G.B. is an advisor for Silver Creek Pharmaceuticals. None of the work presented here is related to these commercial interests. The other authors declare no competing interests.

Additional information

Extended data is available for this paper at https://doi.org/10.1038/s44161-025-00755-6.

Supplementary information The online version contains supplementary material available at https://doi.org/10.1038/s44161-025-00755-6.

Correspondence and requests for materials should be addressed to Irfan S. Kathiriya or Benoit G. Bruneau.

Peer review information *Nature Cardiovascular Research* thanks Kenneth Chien, Joshua Wythe and the other, anonymous, reviewer(s) for their contribution to the peer review of this work.

[1]Department of Anesthesia and Perioperative Care, University of California, San Francsisco, San Francisco, CA, USA. [2]Gladstone Institutes, San Francisco, CA, USA. [3]Department of Medicine, University of California, San Francisco, San Francisco, CA, USA. [4]Department of Chemical and Biomolecular Engineering, Johns Hopkins University, Baltimore, MD, USA. [5]Sol Goldman Pancreatic Cancer Research Center, Department of Pathology, Johns Hopkins University, Baltimore, MD, USA. [6]Department of Oncology, Johns Hopkins University, Baltimore, MD, USA. [7]Department of Functional Anatomy and Evolution, Johns Hopkins University, Baltimore, MD, USA. [8]Roddenberry Center for Stem Cell Biology and Medicine, Gladstone Institutes, San Francisco, CA, USA. [9]Department of Pediatrics, University of California San Francisco, San Francisco, CA, USA. [10]Cardiovascular Research Institute, University of California, San Francisco, San Francisco, CA, USA. [11]Institute for Human Genetics, University of California, San Francisco, CA, USA. [12]The Eli and Edythe Broad Center for Regeneration Medicine and Stem Cell Research, University of California, San Francisco, CA, USA. [13]Present address: Department of Medicine, Drexel College of Medicine, Philadelphia, PA, USA. [14]Present address: Department of Pathology, University of California, San Francisco, San Francisco, CA, USA. [15]Present address: Creighton University School of Medicine, Omaha, NE, USA. [16]Present address: Herman B. Wells Center for Pediatric Research, Indiana University School of Medicine, Indianapolis, IN, USA. [17]Present address: Department of Anesthesiology, Washington University in St. Louis, St. Louis, MO, USA. [18]Present address: Department of Human Genetics, Emory University School of Medicine, Atlanta, GA, USA. [19]Present address: Department of Interventional Radiology, University of Utah School of Medicine, Salt Lake City, UT, USA. [20]Present address: California Institute of Technology, Pasadena, CA, USA. [21]These authors jointly supervised this work: Irfan S. Kathiriya, Benoit G. Bruneau. [22]Deceased: Tatyana Sukonnik. ✉e-mail: irfan.kathiriya@ucsf.edu; benoit.bruneau@gladstone.ucsf.edu

https://doi.org/10.1038/s44161-025-00755-6

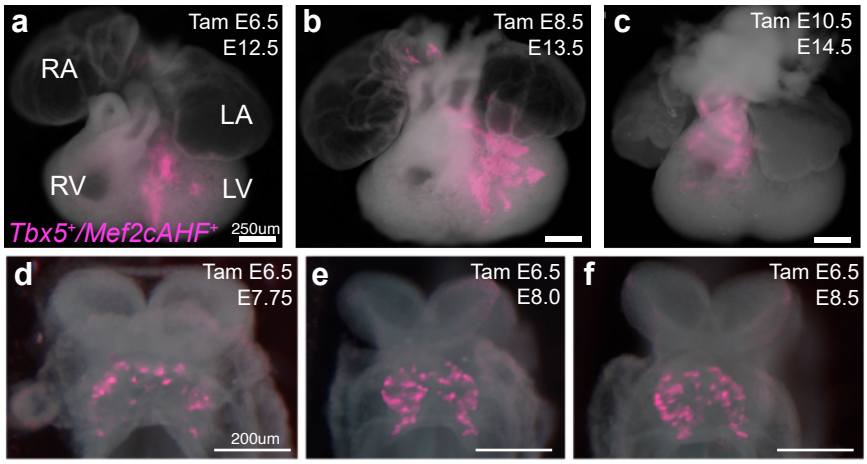

Extended Data Fig. 1 | Time course of progenitors or early contributions of the *Tbx5*$^{+}$/*Mef2cAHF*$^{+}$ lineage. a–**c**, *Tbx5*$^{+}$/*Mef2cAHF*$^{+}$ lineage contributions to the interventricular septum were descendants from progenitors labeled at (**a**) E6.5, but not at (**b**) E8.5 or (**c**) E10.5 in *Tbx5*$^{CreERT2/+}$;*Mef2cAHF-DreERT2*; *ROSA26*$^{Ai6/Ai66}$ embryos. Scale bars: 250 microns. **d**, **e**, Epifluorescence microscopy images of the *Tbx5*$^{+}$/*Mef2cAHF*$^{+}$ lineage (tdTomato immunostaining) labeled by a single dose of tamoxifen at E6.5 of embryos at (**d**) E7.75, (**e**) E8.0 and (**f**) E8.5 displayed an apparent "salt and pepper" pattern in the early developing heart. Scale bars: 200 microns.

https://doi.org/10.1038/s44161-025-00755-6

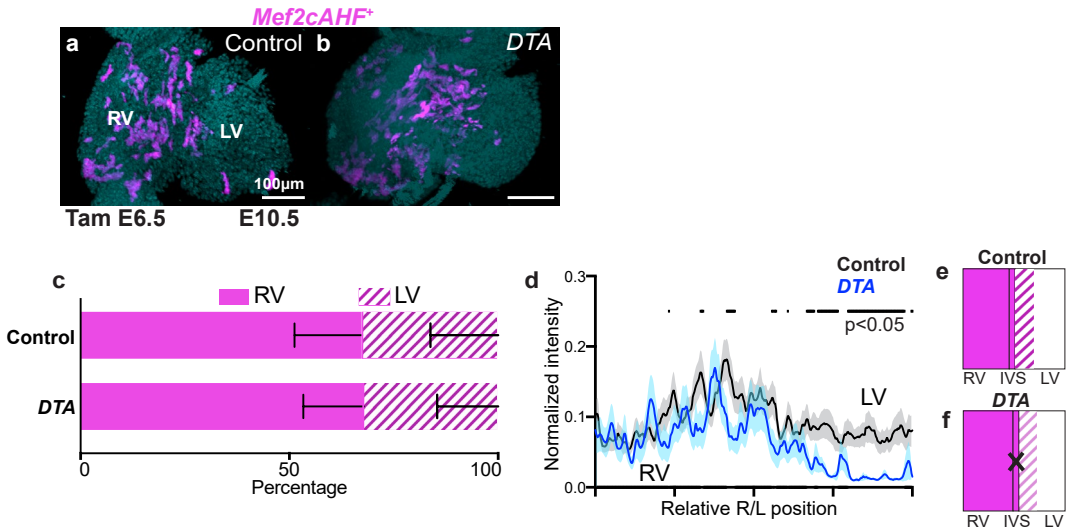

Extended Data Fig. 2 | *Mef2cAHF*$^{+}$ lineage distribution in intersectional-*DTA* mutants. a, *Mef2cAHF*$^{+}$ lineage was enriched in the RV of control embryos (*Tbx5*$^{CreERT2/+}$;*Mef2cAHF-DreERT2;Hip11*$^{+/+}$) (n = 3) and (**b**) intersectional-*DTA* mutant embryos (*Tbx5*$^{CreERT2/+}$;*Mef2cAHF-DreERT2;Hip11*$^{Intersectional\text{-}DTA176/+}$) (n = 2). **c**, This distribution of the *Mef2cAHF*$^{+}$ lineage was not different in the RV or LV between control and *DTA* mutants (p = 0.939327, by two-sided T-test). Cells of the right ventricle (RV) or left ventricle (LV) in five optical slices at different anterior-posterior planes per embryonic heart sample of 3 controls and 2 mutants were evaluated. Mean and standard deviation are shown. **d**, Linear profiles showed a reduction of fluorescence activity in the LV of *DTA* mutants. Linear profiles at 5 apical-basal planes per optical slice, for 5 optical slices at different anterior-posterior planes per embryonic heart sample of 3 controls and 2 *DTA* mutants were assessed. Statistical significance ($p < 0.05$) between linear profiles of control and *DTA* mutants was determined by Welch's two-sided t-test at each position along the right-left axis. Mean and standard error of the mean are shown. Precise p-values can be found in the Source data. **e**, **f**, Cartoon depictions.

https://doi.org/10.1038/s44161-025-00755-6

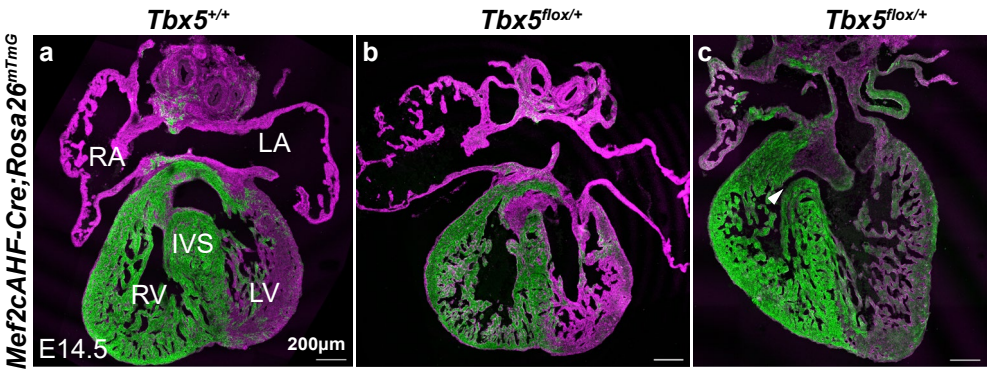

Extended Data Fig. 3 | Conditional haploinsufficiency of *Tbx5* in the interventricular septum (IVS) leads to ventricular septal defects (VSDs). a–**c**, At E14.5, membranous VSDs were observed in *Mef2cAHF-Cre;ROSA26*$^{mTmG/+}$*;Tbx5*$^{flox/+}$ mutant embryos (n = 4/7) compared to *Mef2cAHF-Cre;ROSA26*$^{mTmG/+}$*;Tbx5*$^{+/+}$ controls (n = 0/3). Right ventricle (RV), left ventricle (LV) and interventricular septum (IVS). All scale bars equal 200 microns.

https://doi.org/10.1038/s44161-025-00755-6

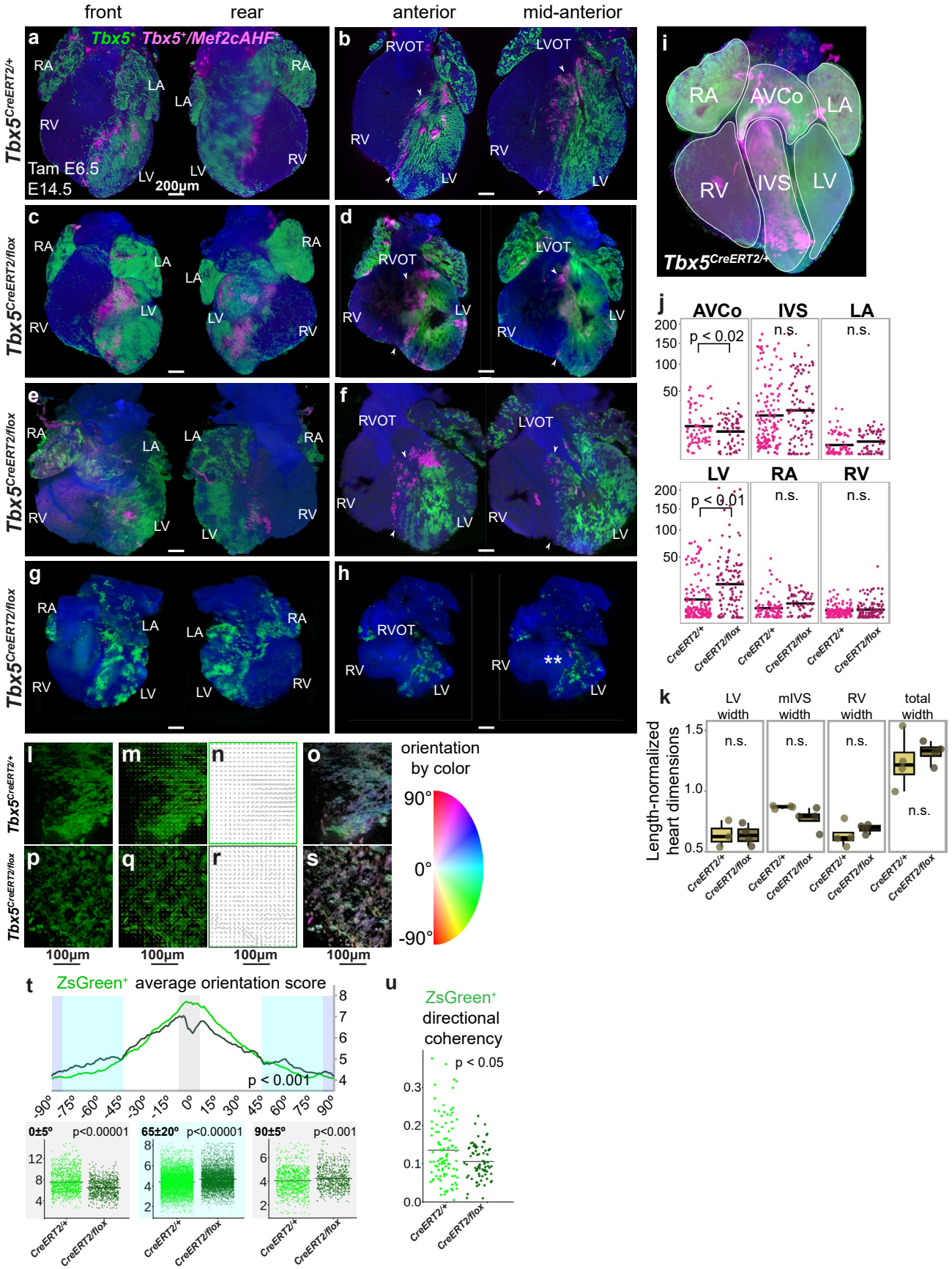

Extended Data Fig. 4 | See next page for caption.

https://doi.org/10.1038/s44161-025-00755-6

Extended Data Fig. 4 | Additional samples of *Tbx5* mutant hearts and supplementary quantification of distribution and cell arrangement. **a**–**h**, Volume renderings from lightsheet microscopy of anterior and posterior surfaces, as well as anterior and mid-anterior 4-chamber optical sections of *Tbx5*$^{CreERT2/+}$ control (*Tbx5*$^{CreERT2/+}$;*Mef2cAHF-DreERT2*;*ROSA26*$^{Ai6/Ai66}$) and *Tbx5*$^{CreERT2/flox}$ mutant (*Tbx5*$^{CreERT2/flox}$;*Mef2cAHF-DreERT2*;*ROSA26*$^{Ai6/Ai66}$) hearts at E14.5 display *Tbx5*$^{+}$ lineage (ZsGreen) and *Tbx5*$^{+}$/*Mef2cAHF*$^{+}$ lineage (tdTomato immunostaining) cells. (**a**-**h**) scale bars: 200 microns. **i**–**k**, Quantification of the anatomical location of tdTomato^{+} and ZsGreen^{+} cells in *Tbx5*$^{CreERT2/flox}$ mutants (n = 3) and *Tbx5*$^{CreERT2/+}$ controls (n = 4), by region at E14.5 as outlined in (**i**). Over 1200 3-dimensional regions of interest were drawn blinded, and then integrated fluorescence signal was assessed. **j**, Although no regional differences in the intensities of ZsGreen^{+} were detected, tdTomato^{+} displayed higher integrated fluorescence in the left ventricle (LV) and less signal in atrioventricular complex (AVCo) complex region by two-sided unpaired T-tests (AVCo: p = 0.01933, interventricular septum (IVS): p = 0.3679, left atrium (LA): p = 0.2829, LV: p = 0.0001574, right atrium (RA): p = 0.1678, right ventricle (RV): p = 0.05063). **k**, Length-normalized widths of LV, muscular IVS (mIVS), RV and total heart at E14.5 were not significantly different between control (n = 4) and *Tbx5* mutants (n = 3) based on regions of interest in (**i**), by two-sided unpaired T-tests (p = 0.9654, 0.1277, 0.3797, 0.5631 for left-to-right plots). Median, first and third quartiles are shown in box plots. Further details are in Source data. **l**–**u**, *Tbx5*$^{CreERT2/flox}$ mutant hearts at E14.5 scored worse for orientation scores of *Tbx5*$^{+}$ lineage (ZsGreen^{+}) cells in the dominant direction (range from -5 to 5 degrees) and scored higher in the orientation orthogonal to the dominant direction (range from 85 to 95 degrees and -85 to -95 degrees), as determined (**t**) by two-sided Watson U2 test across all orientations (p < 0.001) or by two-sided Wilcoxon rank sum test with continuity correction for selected orientations (p-values < 2.2e-16 for left and middle plots, p-value = 0.0006863 for right plots). **u**, *Tbx5*$^{+}$ lineage (ZsGreen^{+}) cells demonstrated worse directional coherency scoring in *Tbx5*$^{CreERT2/flox}$ mutants by two-sided Wilcoxon rank sum test with continuity correction (p = 0.03316). (**l**-**s**) scale bars are 100 microns.

https://doi.org/10.1038/s44161-025-00755-6

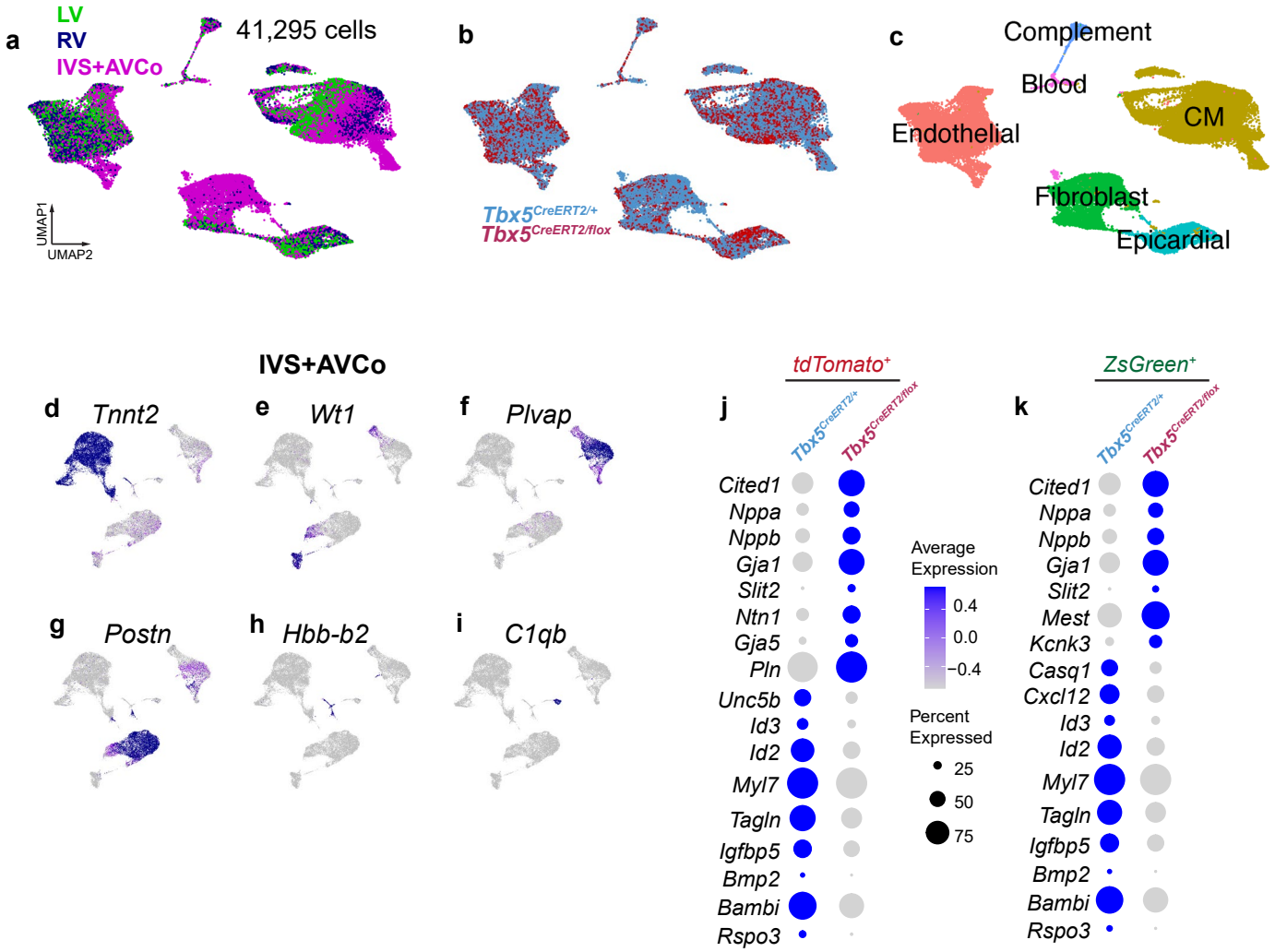

Extended Data Fig. 5 | scRNA-seq of *Tbx5* mutants by region. a–**c**, In scRNA-seq samples from E13.5 hearts, we display cells by (**a**) region (left ventricle (LV), right ventricle (RV), interventricular septu (IVS)) (**b**) genotype, or (**c**) cell types by Louvain clustering. In IVS+atrioventricular complex (AVCo) regions (control, n = 4, *Tbx5* mutant, n = 2), we detected clusters enriched for (**d**) *Tnnt2*$^+$ cardiomyocytes (CMs), (**e**) *Tbx18*$^+$/*Wt1*$^+$ epicardial cells, (**f**) *Plvap*$^+$ endothelial cells, (**g**) *Postn*$^+$ fibroblasts, (**h**) *Hbb-b2*$^+$ red blood cells, and (**i**) *C1qb*$^+$ white blood cells. Dot plots of selected differentially expressed genes in (**j**) *tdTomato*$^+$ or (**k**) *ZsGreen*$^+$ cells from the IVS+AVCo region. Significance of adj $p < 0.05$ was determined by two-sided Wilcoxan rank sum.

https://doi.org/10.1038/s44161-025-00755-6

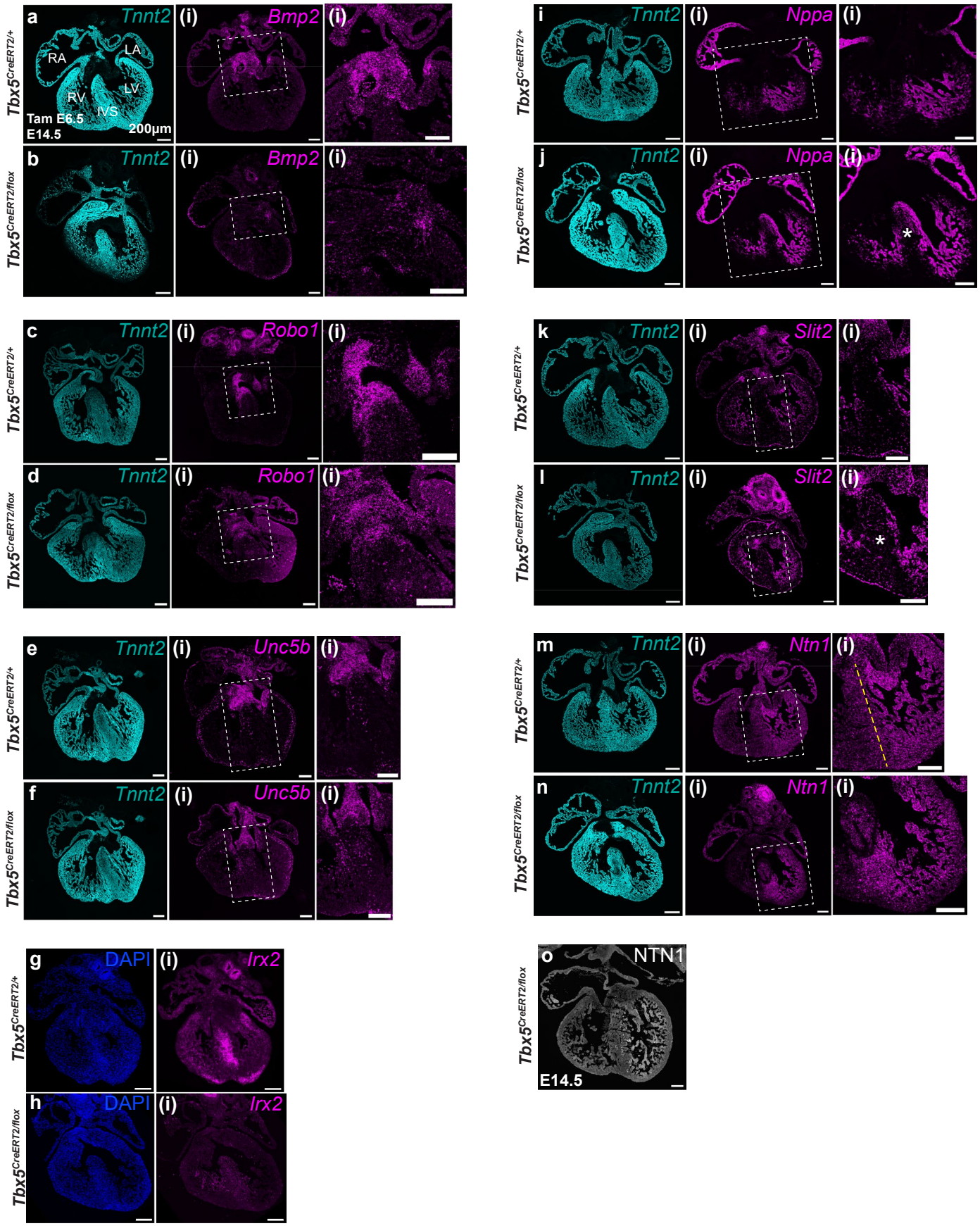

Extended Data Fig. 6 | See next page for caption.

https://doi.org/10.1038/s44161-025-00755-6

Extended Data Fig. 6 | Fluorescent *in situ* hybridization of *Tbx5*-dependent genes at E14.5. a–f”, By fluorescent *in situ* hybridization at E14.5 after a single dose of tamoxifen at E6.5, *Bmp2*, *Robo1* and *Unc5b* are expressed in the atrioventricular canal (boxed region) in $Tbx5^{CreERT2/+}$ controls ($Tbx5^{CreERT2/+}$;*Mef2cAHF-DreERT2*; $ROSA26^{Ai6/Ai66}$), and expression of these genes are reduced in $Tbx5^{CreERT2/flox}$ mutants ($Tbx5^{CreERT2/flox}$;*Mef2cAHF-DreERT2*;$ROSA26^{Ai6/Ai66}$). *Tnnt2* is expressed in cardiomyocytes. **g–h’**, *Irx2* is reduced in the IVS of *Tbx5* mutants. **i–n”**, *Nppa*, *Slit2* and *Ntn1* are expressed in the trabecular layer in $Tbx5^{CreERT2/+}$ controls, and misexpressed in the IVS in $Tbx5^{CreERT2/flox}$ mutants with a membranous VSD at E14.5. Yellow dashed line demarcates gradient of *Ntn1* expression across the IVS from left to right. **o**, Immunostaining of NTN1 at E14.5. All scale bars are 200 microns.

https://doi.org/10.1038/s44161-025-00755-6

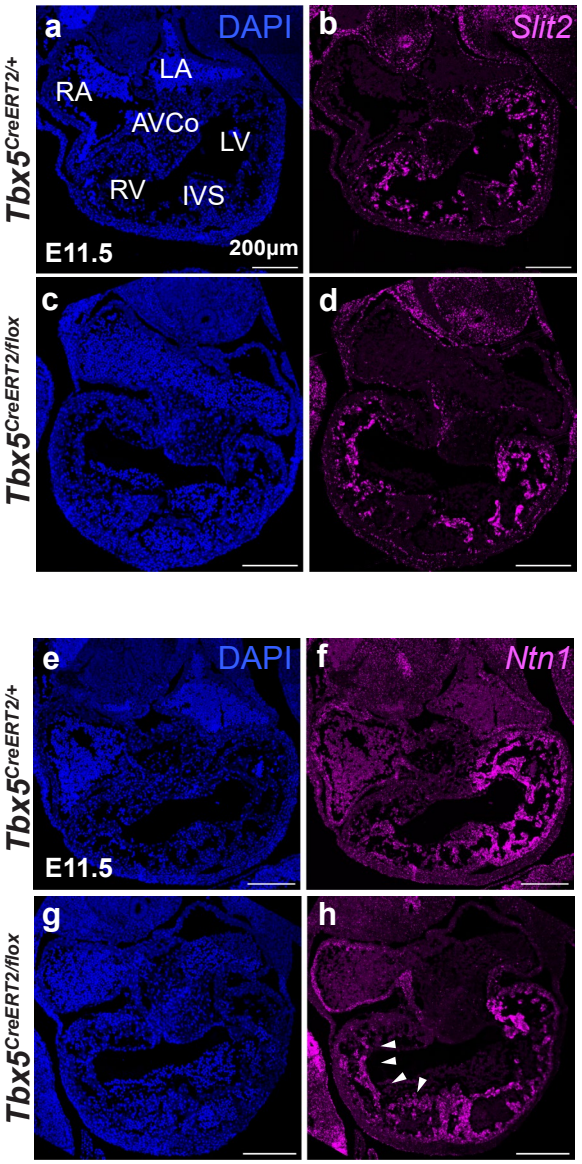

Extended Data Fig. 7 | Expression of *Slit2* and *Ntn1* in *Tbx5* mutants at E11.5. Fluorescent *in situ* hybridization of (**a**–**d**) *Slit2* and (**e**–**h**) *Ntn1* at E11.5 in $Tbx5^{CreERT2/+}$ controls ($Tbx5^{CreERT2/+}$;*Mef2cAHF-DreERT2*;$ROSA26^{Ai6/Ai66}$) and $Tbx5^{CreERT2/flox}$ mutant ($Tbx5^{CreERT2/flox}$;*Mef2cAHF-DreERT2*;$ROSA26^{Ai6/Ai66}$) hearts. Arrowheads highlight ectopic expression of *Ntn1* in the RV. All scale bars are 200 microns.

https://doi.org/10.1038/s44161-025-00755-6

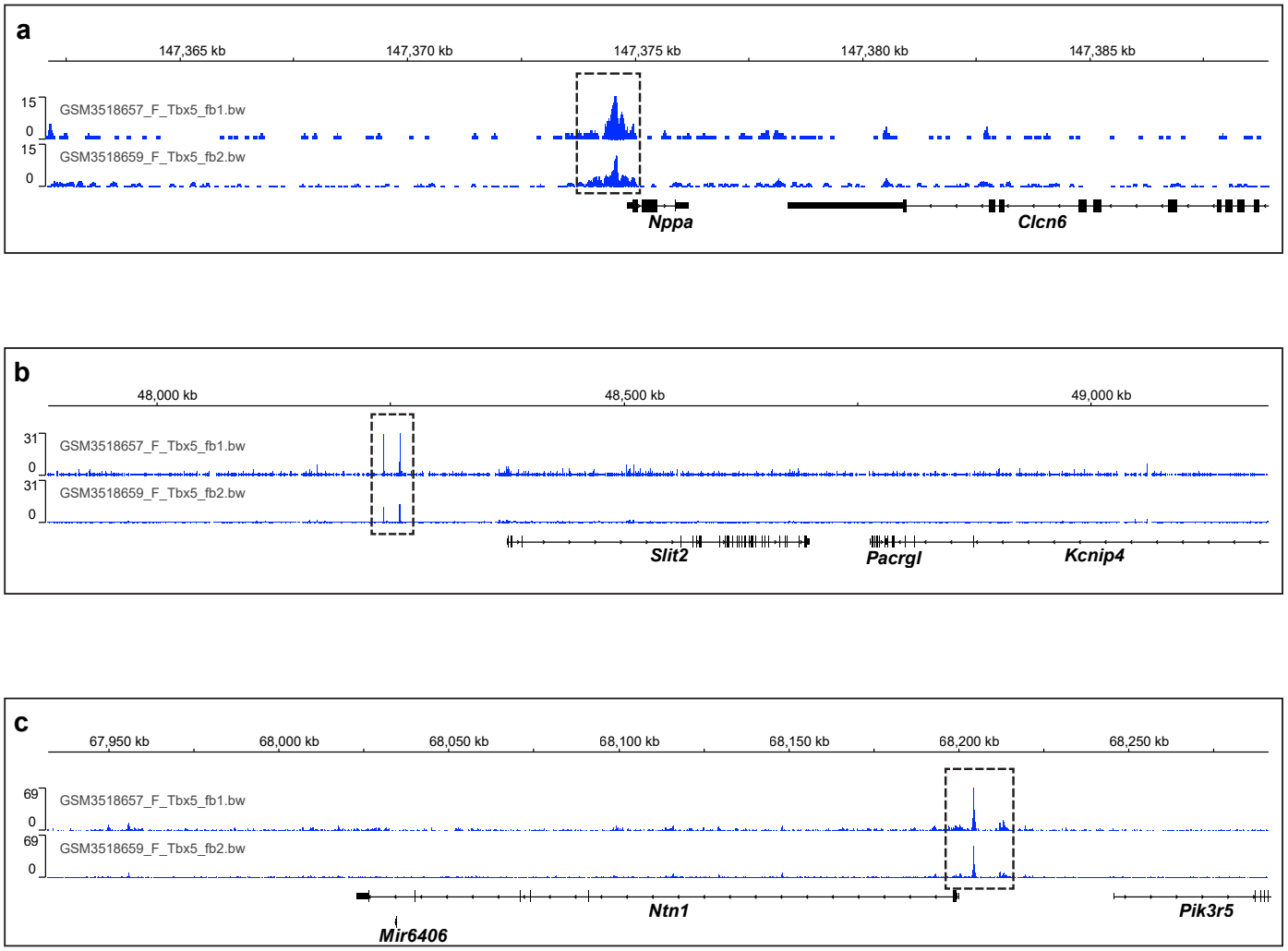

Extended Data Fig. 8 | TBX5 chromatin occupancy near *Slit2* and *Ntn1*. **a**–**c**, Browser tracks of TBX5 ChIP-seq from E12.5 hearts[55] show peaks of TBX5 occupancy (dashed black boxes) near promoters of *Nppa*, *Slit2* and *Ntn1*.

https://doi.org/10.1038/s44161-025-00755-6

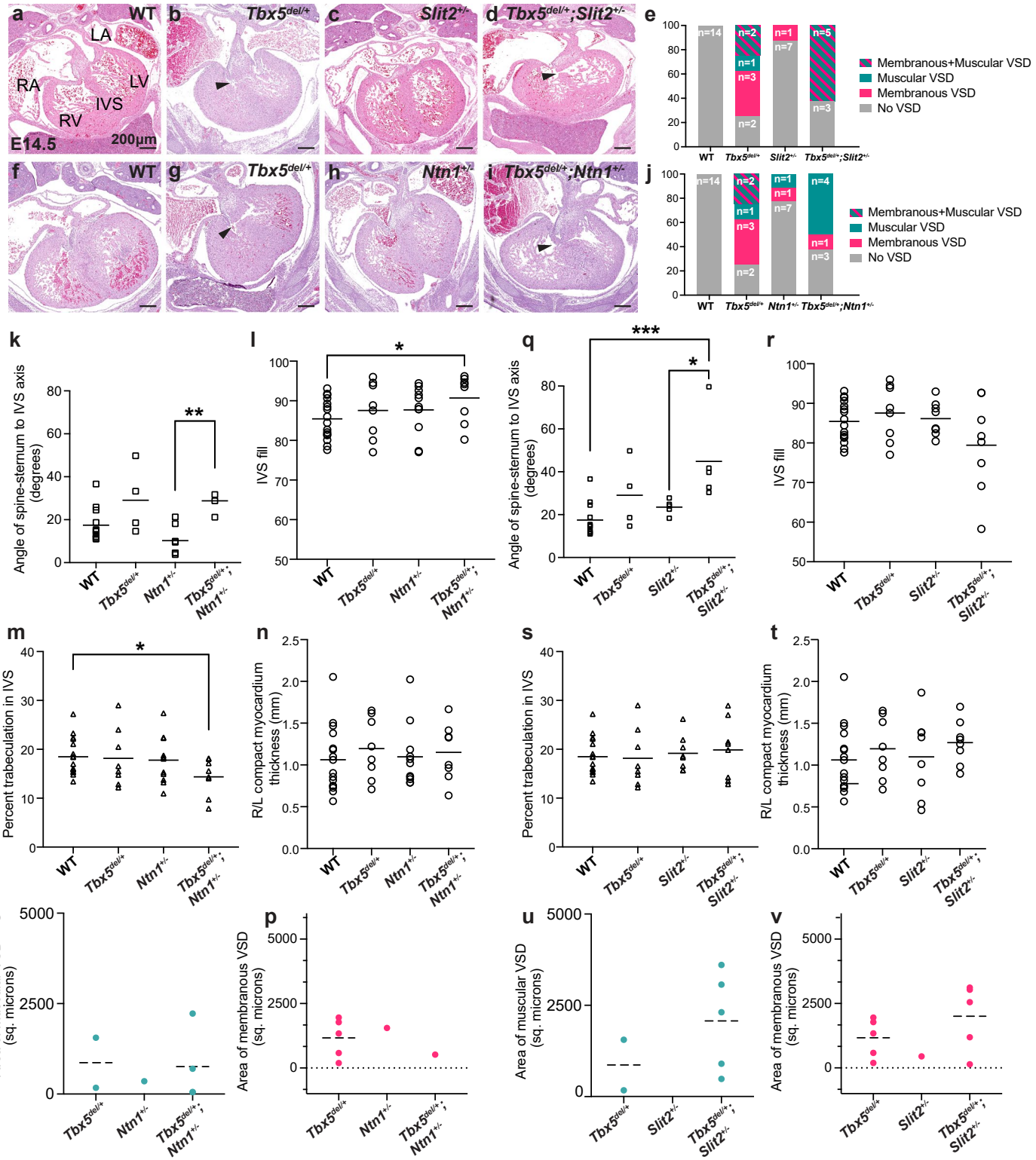

Extended Data Fig. 9 | *Tbx5-Ntn1* and *Tbx5-Slit2* genetic interactions. Histology from E14.5 embryos from matings of (**a**–**d**) $Tbx5^{del/+}$ and $Slit2^{+/-}$ or (**f**–**i**) $Tbx5^{del/+}$ and $Ntn1^{+/-}$ by genotype. Arrowheads depict muscular ventricular septal defects (VSDs). **e**, Quantification of membranous or muscular VSDs by genotype. $Tbx5^{del/+};Slit2^{+/-}$ compound heterozygous embryos displayed an estimated decrease in the incidence of membranous VSDs, which approached significance (log OR -2.5; p = 0.09 in a Generalized Linear Model without adjustments for multiple comparisons). This decrease was relative to the expected incidence of membranous VSDs if there was no genetic interaction between *Tbx5* and *Slit2*. **j**, $Tbx5^{del/+};Ntn1^{+/-}$ compound heterozygous embryos displayed a decrease of membranous VSDs (log OR -5.3; $p = 1\times10^{-3}$ by a Generalized Linear Model without adjustments for multiple comparisons), relative to the expected incidence of membranous VSDs if there was no genetic interaction between *Tbx5* and *Ntn1*, but not changes to prevalence of muscular VSDs (log OR 0.12; p = 0.93). **k**–**v**, Machine-learning based quantitative morphometry of metrics for (k-p) $Tbx5^{del/+}$ and $Ntn1^{+/-}$ or (q-v) $Tbx5^{del/+}$ and $Slit2^{+/-}$ by genotype. IVS, interventricular septum. Significance determined by two-sided Fisher's exact test (*p < 0.05, **p < 0.01, ***p < 0.001). (k) **p = 0.0059, (l)*p = 0.0337, (m) *p = 0.0196, (q)***p = 0.0008, *p = 0.0468. All scale bars are 200 microns.

https://doi.org/10.1038/s44161-025-00755-6

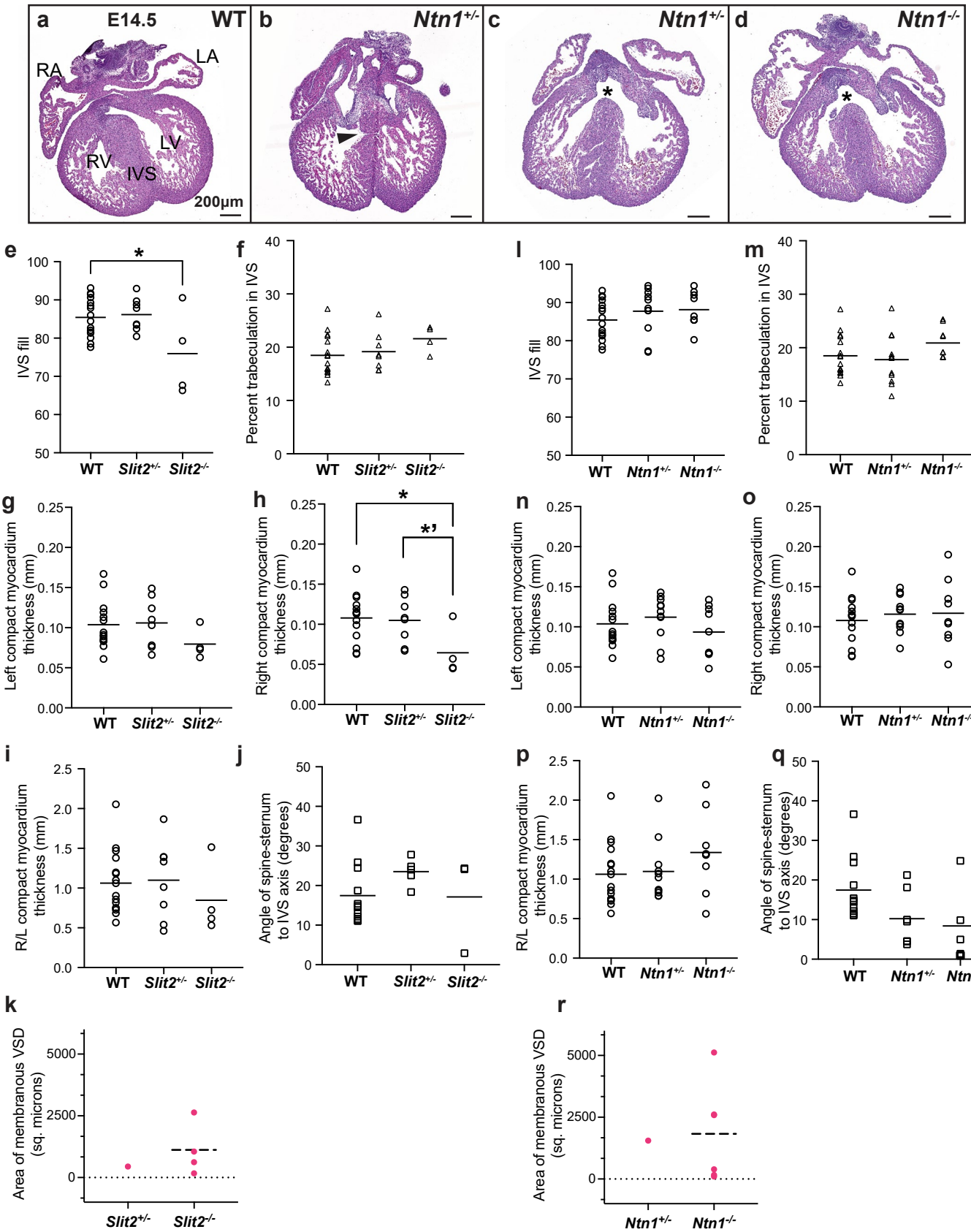

Extended Data Fig. 10 | Quantitative morphometry of *Slit2* and *Ntn1* mutant hearts. a–**d**, Additional histology by *Ntn1* genotype at E14.5. Arrowhead, muscular ventricular septal defect (VSD). Asterisk, membranous VSD. Scale bars are 200 microns. **e**–**p**, Machine learning-based quantitative cardiac morphometrics for (**e**–**k**) *Slit2* or (**l**–**r**) *Ntn1* mutants. Significance determined by two-sided Fisher's exact test (*p < 0.05). **k**, **r**, Morphometry of the area of membranous VSDs by *Slit2* or *Ntn1* genotypes. (E) *p = 0.0184, (H) *p = 0.0216, *'p = 0.0492.

nature portfolio

Corresponding author(s): Kathiriya, Bruneau

Last updated by author(s): October 31, 2025

Reporting Summary

Nature Portfolio wishes to improve the reproducibility of the work that we publish. This form provides structure for consistency and transparency in reporting. For further information on Nature Portfolio policies, see our Editorial Policies and the Editorial Policy Checklist.

Statistics

For all statistical analyses, confirm that the following items are present in the figure legend, table legend, main text, or Methods section.

n/a	Confirmed	
☐	☒	The exact sample size (*n*) for each experimental group/condition, given as a discrete number and unit of measurement
☐	☒	A statement on whether measurements were taken from distinct samples or whether the same sample was measured repeatedly
☐	☒	The statistical test(s) used AND whether they are one- or two-sided *Only common tests should be described solely by name; describe more complex techniques in the Methods section.*
☒	☐	A description of all covariates tested
☐	☒	A description of any assumptions or corrections, such as tests of normality and adjustment for multiple comparisons
☐	☒	A full description of the statistical parameters including central tendency (e.g. means) or other basic estimates (e.g. regression coefficient) AND variation (e.g. standard deviation) or associated estimates of uncertainty (e.g. confidence intervals)
☐	☒	For null hypothesis testing, the test statistic (e.g. *F*, *t*, *r*) with confidence intervals, effect sizes, degrees of freedom and *P* value noted *Give P values as exact values whenever suitable.*
☒	☐	For Bayesian analysis, information on the choice of priors and Markov chain Monte Carlo settings
☒	☐	For hierarchical and complex designs, identification of the appropriate level for tests and full reporting of outcomes
☒	☐	Estimates of effect sizes (e.g. Cohen's *d*, Pearson's *r*), indicating how they were calculated

Our web collection on statistics for biologists contains articles on many of the points above.

Software and code

Policy information about availability of computer code

Data collection	We used Aperia Versa software with the Leica Versa 200 Automated Slide Scanner to acquire images of serial sections. Zen software with the Zeiss Lightsheet Z.1, additional details for lightsheet image preprocessing is found in Methods; RNAscope image stitching using the Olympus FV3000RS software, Cellranger 2.02 (10X Genomics) for read alignments and Cellaggr for read depth normalization.
Data analysis	Outputs from the Cellranger pipeline were analyzed using the Seurat v3 (Stuart et al., 2019), ImageJ (several plugins are noted in Methods), Code related to "Image Volume Quantification" (Dominguez et al., 2023) is available at https://github.com/mhdominguez/LSFMProcessing. Source data and scripts used to analyze other morphometrics from light sheet microscopy, such as right-left positioning, orientation and directionality of cells, are available at github.com/mhdominguez/Kathiriya-NCVR-2025-analysis. MatLab (Mathworks) for implementing CODA (Kiemen et al., 2022).

For manuscripts utilizing custom algorithms or software that are central to the research but not yet described in published literature, software must be made available to editors and reviewers. We strongly encourage code deposition in a community repository (e.g. GitHub). See the Nature Portfolio guidelines for submitting code & software for further information.

Data

Policy information about availability of data

All manuscripts must include a data availability statement. This statement should provide the following information, where applicable:

- Accession codes, unique identifiers, or web links for publicly available datasets
- A description of any restrictions on data availability
- For clinical datasets or third party data, please ensure that the statement adheres to our policy

Source data is included by Figure. scRNA-seq data generated in this paper is available in the NCBI GEO database (GSE260601). ChIP-seq data from Akerberg et al., 2019, is available in the GEO database (GSE124008).

Research involving human participants, their data, or biological material

Policy information about studies with human participants or human data. See also policy information about sex, gender (identity/presentation), and sexual orientation and race, ethnicity and racism.

Reporting on sex and gender	This study did not involve human subjects.
Reporting on race, ethnicity, or other socially relevant groupings	*Please specify the socially constructed or socially relevant categorization variable(s) used in your manuscript and explain why they were used. Please note that such variables should not be used as proxies for other socially constructed/relevant variables (for example, race or ethnicity should not be used as a proxy for socioeconomic status).* *Provide clear definitions of the relevant terms used, how they were provided (by the participants/respondents, the researchers, or third parties), and the method(s) used to classify people into the different categories (e.g. self-report, census or administrative data, social media data, etc.)* *Please provide details about how you controlled for confounding variables in your analyses.*
Population characteristics	*Describe the covariate-relevant population characteristics of the human research participants (e.g. age, genotypic information, past and current diagnosis and treatment categories). If you filled out the behavioural & social sciences study design questions and have nothing to add here, write "See above."*
Recruitment	*Describe how participants were recruited. Outline any potential self-selection bias or other biases that may be present and how these are likely to impact results.*
Ethics oversight	*Identify the organization(s) that approved the study protocol.*

Note that full information on the approval of the study protocol must also be provided in the manuscript.

Field-specific reporting

Please select the one below that is the best fit for your research. If you are not sure, read the appropriate sections before making your selection.

☒ Life sciences ☐ Behavioural & social sciences ☐ Ecological, evolutionary & environmental sciences

For a reference copy of the document with all sections, see nature.com/documents/nr-reporting-summary-flat.pdf

Life sciences study design

All studies must disclose on these points even when the disclosure is negative.

Sample size	No sample size calculations were performed. Duplicates were considered sufficient for statistical robustness in most cases. When feasible, additional samples were collected and analyzed.
Data exclusions	One Tbx5 mutant sample of the IVS+AVC was not included because it was lost from a microfluidic clog during sample processing.
Replication	Samples were allocated based on embryonic stage or genotype. Multiple replicates and orthogonal experiments, such as fluorescence in situ hybridization, were used to verify the reproducibility of the scRNAseq. Representative images are shown based on experiments that were repeated independently with similar results, as follows: Figure(s) 1a-f: 2 samples; 1g-j: 5 samples; 2a-i: 4 samples; 2j-n: 6 samples; 2o-q: 8 samples; 2r-t: 15 samples; 3a,b: 2 controls, 2 DTA mutants; 3c-j: 2 controls, 4 DTA mutants; 3l-n' and Extended Data 2: 3 controls, 2 DTA mutants; 4a-d: 5 controls and 4 Tbx5 mutants, for which some samples are shown in Extended Data Figure 4a-i; Figure 4i-m: 4 controls, 4n-r: 3 Tbx5 mutants; 4u-v'; 2 controls, 2 Tbx5 mutants; 5i-n; 2 controls and 2 Tbx5 mutants, for which the second replicates are shown in Extended Data Figure 6i-n"; Figure 6f-h: 14 controls, 8 Slit2+/-, 4 Slit2-/-; 6j-l: 14 controls, 9 Ntn1+/-, 7 Ntn1-/-, with some samples shown in Extended Data Figure 10a-d; Extended Data Figure(s) 1: 2 samples per condition; 4a-l: 5 controls, 4 Tbx5 mutants, with some samples shown in Figure 4; 3: 3 controls, 7 Tbx5 mutants; 6a-h': 2 controls and 2 Tbx5 mutants; 6o: 2 controls; 7a-h: 2 controls and 2 Tbx5 mutants; 9a-d: 14 controls, 8 Tbx5+/-, 8 Slit2+/-; 8 Tbx5+/-;Slit2+/-; 9f-i: 14 controls, 7 Tbx5+/-; 9 Ntn1+/-, 7 Ntn1-/-. Supplemental Figure(s) 1: 5 samples; 2: 5 controls, 4 Tbx5 mutants; 3: 2 controls, 2 Tbx5 mutants. Number of replicates are denoted for each graph in figure legends. Several limitations of this study should be considered. Using inducible genetic tracing, there is an inherent variability from recombination of the fluorescent reporters within samples. For some comparisons, more samples of each genotype could have mitigated this limitation, but obtaining additional samples have been technically challenging, in large part due to a requirement of 5 alleles to be present. Notwithstanding, we have tried to account for recombination efficiency, when possible, in imaging analyses. We have made great effort to mitigate this concern by not quantifying

measurements that would be greatly skewed by recombination efficiency. For this reason, for example, we have refrained from commenting on whether a given lineage is quantitatively increased or decreased if fewer samples were available. Instead, we have focused our analyses on the location of the cells, as we feel that this is less affected by recombination efficiency. Using orthogonal approaches, we measure in an unbiased and statistically robust fashion using various metrics of quantitative morphometry from lightsheet or histology images. Our interpretations are based on statistical robustness from a large number of sampled regions per embryo, in the comparisons that are presented. The repeated measurements are akin to the (much larger) measurements in single cell RNAseq.

Randomization: Randomization was not relevant to the design of this study.

Blinding: Blinding was used for qualitative assessment and quantitative morphometry.

Reporting for specific materials, systems and methods

We require information from authors about some types of materials, experimental systems and methods used in many studies. Here, indicate whether each material, system or method listed is relevant to your study. If you are not sure if a list item applies to your research, read the appropriate section before selecting a response.

Materials & experimental systems

n/a	Involved in the study
☐	☒ Antibodies
☒	☐ Eukaryotic cell lines
☒	☐ Palaeontology and archaeology
☐	☒ Animals and other organisms
☒	☐ Clinical data
☒	☐ Dual use research of concern
☒	☐ Plants

Methods

n/a	Involved in the study
☒	☐ ChIP-seq
☒	☐ Flow cytometry
☒	☐ MRI-based neuroimaging

Antibodies

Antibodies used: Primary antibodies used were: tdTomato (rabbit, Rockland 600-401-379, 1:1000), MEF2c (sheep, R&D AF6786, 1:250)(Dominguez et al., 2023), TNNT2 (mouse, Thermo MS-295-P, 1:500)(Kathiriya et al., 2021), Netrin-1 antibody 1:500 (R&D Systems AF1109) (Ramkhelawon et al., 2014).

Validation: Selection of antibodies were based on validation in previous publications.

Animals and other research organisms

Policy information about studies involving animals; ARRIVE guidelines recommended for reporting animal research, and Sex and Gender in Research

Laboratory animals: Mice were housed in a barrier animal facility with standard husbandry conditions (dark/light cycle, ambient temperature and humidity) at the Gladstone Institutes. Mice of Tbx5CreERT2IRES2xFLAG (abbreviated here as Tbx5CreERT2) and Mef2cAHF-DreERT2 25, Tbx5del/+ and Tbx5flox/+ 45, ROSA26Ai66 and ROSA26Ai6 35 were described previously. Mef2cAHF-Cre mice 46 were obtained from Brian Black (University of California, San Francisco). Slit2+/- mice (MMRC, Strain 065588-UCD, donated by Kent Lloyd, UC Davis) were generated by CRISPR/Cas9-targeted constitutive deletion of exon 8 and flanking splicing regions of Slit2. Ntn1+/- mice were derived from matings of Ntn1 floxed mice (Ntn1flox/+; Jackson Laboratory #028038) 56 to beta-actin-Cre 57, which were obtained from Gail Martin (University of California, San Francisco). All mouse strains were maintained in the C57BL6/J background (Jackson Laboratory #664), except for Tbx5del/+, which was maintained in Black Swiss (Charles River, Strain Code 492), and Slit2+/- which was maintained in C57BL6/N (Jackson Laboratory, #005304). Both male and female embryos were collected from timed matings and used at random for experiments. We generated an attenuated diptheria toxin (DTA176) transgenic knock-in mouse under the control of the dual-recombinase intersectional cassette. Figure(s) 1a-f: Embryonic day (E) 14.5; 1g-j: E14.5; 2a-i: E8.0; 2j-n: E8.25; 2o-q: E8.5 2r-t: E10.5; 3a,b: E9.5; 3c-j: E12.5; 3l-n' and Extended Data 2: E10.5; 4a-d: E14.5; Figure 4i-m: E14.5, 4n-r: 3E14.5; 4u-v'; 2E14.5; 5i-n; E14.5; Figure 6f-h: E14.5; Extended Data Figure(s) 1: E12.5 (a), E13.5 (b), E14.5 (c), E7.75 (d), E8.0 (e), E8.5 (f); 3: E14.5; 4a-l: E14.5; 5: E13.5, 6a-h': E14.5; 6o: E14.5; 7a-h: E11.5; 9a-d: E14.5; 9f-i: E14.5 Supplemental Figure(s) 1: E10.5; 2: E14.5; 3: E14.5.

Wild animals: The study did not involve wild animals.

Reporting on sex: Sex-based information was not collected for embryonic specimens.

Field-collected samples: The study did not involve samples collected in the field.

Ethics oversight: All mouse protocols were approved (AN203375-00H and AN199784-00E) by the Institutional Animal Care and Use Committee at UCSF.

Note that full information on the approval of the study protocol must also be provided in the manuscript.

Plants

Seed stocks

The study does not involve plants.

Novel plant genotypes

Describe the methods by which all novel plant genotypes were produced. This includes those generated by transgenic approaches, gene editing, chemical/radiation-based mutagenesis and hybridization. For transgenic lines, describe the transformation method, the number of independent lines analyzed and the generation upon which experiments were performed. For gene-edited lines, describe the editor used, the endogenous sequence targeted for editing, the targeting guide RNA sequence (if applicable) and how the editor was applied.

Authentication

Describe any authentication procedures for each seed stock used or novel genotype generated. Describe any experiments used to assess the effect of a mutation and, where applicable, how potential secondary effects (e.g. second site T-DNA insertions, mosiacism, off-target gene editing) were examined.